Research Square

Preprints are preliminary reports that have not undergone peer review.
They should not be considered conclusive, used to inform clinical practice,
or referenced by the media as validated information.

Mathematical Analysis of Radiative Darcy-Forchheimer Flow of an Eyring-Powell Nanofluid over a Stretching Cylinder with Convective Heating and Chemical Reaction

Ebba Hindebu Rikitu

ebba.hindebu@astu.edu.et

Adama Science and Technology University

Jima Seyoum Abera

Adama Science and Technology University

Research Article

Keywords: Powell-Eyring fluid, stretching cylinder, MHD, radiation, convective heating, Darcy-Forchheimer, chemical reaction

Posted Date: August 19th, 2026

DOI: https://doi.org/10.21203/rs.3.rs-10250637/v1

License: This work is licensed under a Creative Commons Attribution 4.0 International License.
Read Full License

Additional Declarations: No competing interests reported.

Mathematical Analysis of Radiative Darcy-Forchheimer Flow of an Eyring-Powell Nanofluid over a Stretching Cylinder with Convective Heating and Chemical Reaction

Ebba Hindebu Rikitu[1*] and Jima Seyoum[1]

[1*]Department of Applied Mathematics, Adama Science and Technology University, Oromia, Adama, 1888, Ethiopia.

*Corresponding author(s). E-mail(s): ebba.hindebu@astu.edu.et;
Contributing authors: jima.seyoum@astu.edu.et;

Abstract

The present research paper deals with the analysis of mathematical modeling of Darcy-Forchheimer flow of Eyring-Powell nanofluid over a stretching cylinder under the influence of a magnetic field, thermal radiation, convective boundary condition, chemical reaction, and Cattaneo-Christov heat and mass flux on heat and mass transfer. The resulting nonlinear partial differential equations are transformed into ordinary differential equations through similarity transformations. The derived equations are then solved through the Homotopy Analysis Method (HAM) with the aid of mathematical software. The effects of the various physical parameters on the velocity, thermal, and concentration profiles are analyzed and discussed in light of the various transport phenomena involved. It is observed that the velocity profile is inversely proportional to the values of the Darcy number and magnetic parameter, whereas an increase in the value of the Eyring-Powell fluid parameter and curvature parameter increases the velocity profile. It is also found that there is an inverse relationship between the temperature profile in the boundary layer and the value of the thermal relaxation time parameter (λ_t). Furthermore, an increase in the value of the Eyring-Powell fluid parameter leads to a reduction in the value of both the skin-friction coefficient and the Nusselt number. Lastly, the results given presently correspond in good agreement with the literature currently in publication.

Keywords: Powell-Eyring fluid; stretching cylinder; MHD; radiation; convective heating; Darcy-Forchheimer; chemical reaction

1 Introduction

The study of boundary layer flow has great significance in fluid mechanics, where the viscous flow of fluid adjacent to a solid surface, i.e., the frictional layer, is studied. As per the boundary layer theory of Prandtl presented in 1904, the effect of viscosity forces predominates within the thin layer near the solid surface due to the presence of velocity gradient within the thin layer, while it can be ignored outside the thin layer. The major application areas of boundary layer theory lie in calculating the frictional drag on the bodies immersed in a fluid medium, and this includes turbine blades, body of aircraft, airfoil, ships, and zero-angle-of-incidence plates. The study of boundary layer flow over continuously moving solid surface was firstly conducted by [**?**], while [2] was the first researcher to conduct research work on flow over stretching sheet. After these groundbreaking contributions, a number of research works have been conducted in the area of boundary layer flow, and experimental validation of the outcomes has also been done [3, 4]. The heat and mass transfer in boundary layers have significant impact in industries since it has effects on product quality and their production cost.

The behavior of non-Newtonian fluids is described by a non-linear variation between the shear stress and rate of deformation, which are represented by paint, mud, blood, ketchup, and shampoo. Even though the equations involved in non-Newtonian fluids may become very complicated, the mathematical modeling of such fluids has become quite popular recently [5–7]. Ferdows et al.[8] analyzed the thermal effectiveness of cooling due to a non-Newtonian nanofluid flow across a moving expanding sheet with variable power-law index. The study concluded that velocity and temperature gradient decreased after the separation point, whereas the boundary layer thickness increased with increasing free-stream velocity. The Eyring-Powell fluid is a model for the non-Newtonian fluid having nonlinear dependency of shear stress with respect to strain rate. In the same way, the author [9] analyzed the radiation and chemical reaction effects on Eyring-Powell fluid flow by using the generalized heat flux model and found that the Eyring-Powell parameter increased the velocity of the fluid but decreased its temperature. The fluid temperature increases with increasing value of the radiation parameter. Some researchers [10] have worked on different aspects of Eyring-Powell fluid flow. Flow of heat and fluid through porous media has received great attention from researchers during the last decades due to their wide applications.

It is highly essential to analyze the flow of fluids in the Darcy porous media for several important real-life applications such as groundwater flow, water treatment processes, nuclear waste disposal, geothermal energy recovery, and oil recovery operations in the field of chemical, environmental, and biomedical engineering. The analysis of the flow of fluids in the Darcy porous media has been performed by applying Darcy's law. However, the conventional Darcy law has been modified to examine the effect of non-Darcy effects, which have been analyzed under the Darcy-Forchheimer law. Authors [11, 12] have examined the impact of entropy generation on bioconvection Maxwell nanofluid flow past a rotating disk with thermal radiation, Brownian motion, thermophoresis, and Biot number effects. It has been found that an increase in the inertia coefficient and magnetic field leads to a reduction in the velocity profile. Studies [13] were carried out on bioconvection with Darcy-Forchheimer cylindrical geometry for nanofluid flow analysis with biological and physical explanations for microbe concentration, heat and mass transport, and wall friction. From these findings, it was found that curvature plays a positive role in the velocity profile, while Eyring-Powell fluid parameters influence temperature. A decrease in the rate of heat transport is influenced by the thermophoresis effect, Brownian diffusion, and thermal radiation, while wall friction depends on varying Darcy number. Also, Akinbo [14] carried out studies on irreversibility in hydromagnetic flow for porous medium considering the influence of viscous dissipation and thermal buoyancy effect in nonlinearly radiated Walters' B fluid. It was discovered from the findings that temperature distribution decreases since the buoyancy force dominates over the viscous force, thus enhancing cooling of the system; viscous heating increases due to the Brinkman number because of heat transfer due to molecular conduction in the system.

Moreover, the impact of radiation and chemical reactions on the stagnation point flow of hydromagnetic Walters' B fluid with Newtonian heating was explored in [15]. They have concluded that higher values of the radiation parameter increase the radiative flux and thus increase the polymeric flow, while Newtonian heating, i.e., $\gamma > 0$, causes the temperature distribution and hence the thermal effects on the quiescent fluid are significant in the drying process. Reddy et al. [16] have studied the optimization of entropy in magneto-nonlinear mixed convection flow of Ree-Eyring nanofluid with activation energy and gyrotactic microorganisms. They concluded that the axial velocity of Eyring-Powell fluid is decreased due to the magnetic field but increased by the velocity ratio and material parameters. Radiation and chemical reactions interactions of Walters' B fluid through porous medium on a vertical stretching surface, where the study revealed that higher values of the radiation parameter increase the radiative flux, leading to an increase in heat transfer to the fluid and hence increasing the polymeric flow [17]. The heat and mass flux in the Cattaneo-Christov model takes into consideration thermal and solutal relaxation times. In recent years, the importance of the Cattaneo-Christov heat flux model along with heat generation/absorption and chemical reaction in Walters' B fluid through a porous medium with Newtonian heating was established by [18]. The major result obtained here is that the temperature distribution is affected by the Cattaneo-Christov heat flux model, which describes thermal relaxation phenomena and implies that there is a delay in the propagation of heat in the fluid, meaning the time required to transfer the heat into the medium is increased.

The primary objective of this research work is to analyze the effect of viscous dissipation, thermal radiation, the Cattaneo-Christov heat and mass flux model, and non-linear Darcy-Forchheimer resistance on the flow behavior of Eyring-Powell fluid flow over a stretching cylinder. To the best of our knowledge, no previous study has been conducted to investigate the Darcy-Forchheimer flow of Eyring-Powell nanofluid past a stretching cylinder taking into account the aspects of thermal radiation, convective boundary condition, chemical reaction, and Cattaneo-Christov

heat and mass flux model by using the HAM method. In this regard, this study intends to investigate the MHD flow of Darcy Forchheimer radiative Eyring Powell fluid past a stretching cylinder by considering the above factors.

2 Mathematical Formulation

Suppose that the two-dimensional laminar steady incompressible MHD flow of a Darcy-Forchheimer Eyring-Powell nanofluid exists in the boundary layer over a stretching cylinder. The study considers the impacts of thermal radiation, convective heating, chemical reaction, and the Cattaneo-Christov heat and mass flux models on the problem of interest. The energy and concentration equations are established using the two-phase Buongiorno model for nanofluids. A cylindrical polar coordinate system (x, r), as shown in Figure 1, is used to represent the geometry of the flow problem. In this study, the axis r is taken to be perpendicular to the cylindrical surface and the axis x is parallel to the stretching direction of the cylinder. The stretching velocity in the x-direction is given as $v = 0$ and u=$u_0\left(\frac{x}{l}\right)$, whereas the radial velocity component is set to be zero ($v = 0$). Here, $u = u_\infty$ is the free-stream velocity and u_w represents the velocity at the wall. Here, the temperature T_w denotes the fluid temperature at the wall and T_∞ represents the fluid temperature at infinity.

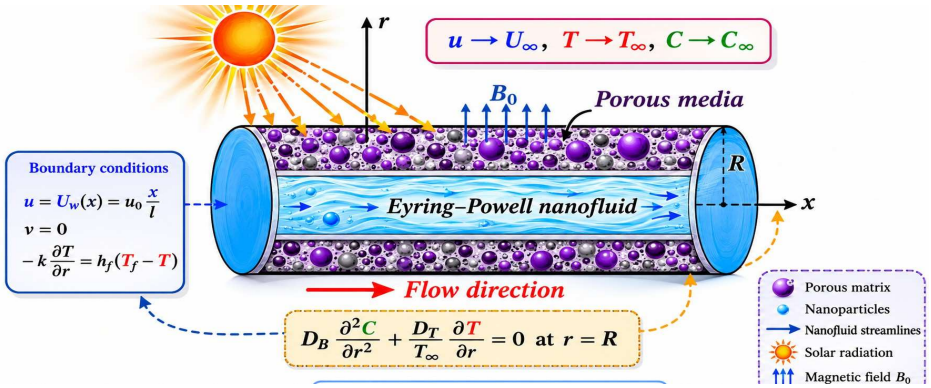


Fig. 1 Flow geometry model.

According to [10], shear stress for the Eyring–Powell model can be expressed as follows

$$\tau_{ij} = \mu\frac{\partial u_i}{\partial x_j} + \frac{1}{\beta}sinh^{-1}\left(\frac{1}{c}\frac{\partial u_i}{\partial x_j}\right) = \mu\frac{\partial u}{\partial r} + \frac{1}{\beta}sinh^{-1}\left(\frac{1}{c}\frac{\partial u}{\partial r}\right). \tag{1}$$

The τ_{ij} is Eyring–Powell fluid's shear stress , u is axial fluid velocity, μ is dynamic viscosity, and β and c are rheological Eyring-Powell model parameters . The second-order approximate Taylor's series grows $sinh^{-1}$ as follows:

$$sinh^{-1}\left(\frac{1}{c}\frac{\partial u}{\partial r}\right) \approx \frac{1}{c}\frac{\partial u}{\partial r} - \frac{1}{3!}\left(\frac{\partial u}{\partial r}\right)^3, \left|\frac{1}{c}\frac{\partial u}{\partial r}\right| \lll 1 \tag{2}$$

Thus, equation 2 taken form as follows:

$$\tau_{ij} = \mu\frac{\partial u}{\partial r} + \frac{1}{\beta c}\frac{\partial u}{\partial r} - \frac{1}{6\beta c^3}\left(\frac{\partial u}{\partial r}\right)^3. \tag{3}$$

The non-Fourier and non-Fick flux models can be combined to formulate the Cattaneo–Christov heat and mass flux model, as proposed by Christov [19].

$$\lambda_E[U.\nabla q - q.\nabla U + (\nabla.U)q] + q = -K\nabla T. \tag{4}$$

$$\lambda_C[U.\nabla J - J.\nabla U + (\nabla.U)J] + J = -D_B \nabla C. \tag{5}$$

For steady incompressible fluid flow, when $\lambda_E = 0$ and $\lambda_C = 0$, Christov's equations reduce to the classical Fourier and Fick laws, respectively.

$$q = -K\nabla T. \tag{6}$$

$$J = -D_B \nabla C. \tag{7}$$

For steady incompressible fluid flow, Equations (4) and (5) reduce to:

$$\lambda_E[U.\nabla q - q.\nabla U] + q = -K\nabla T. \tag{8}$$

$$\lambda_C\,(U \cdot \nabla J - J \cdot \nabla U) + J = -D_B \nabla C. \tag{9}$$

Here, U =(u,v) is the velocity vector of the fluid, q is the heat flux, J is the mass flux, λ_E is the thermal relaxation time, λ_C is the solutal relaxation time, K is the thermal conductivity of the flow, and D_B is the molecular mass diffusivity of the species. In the light of the foregoing discussion, it may be concluded that the non-Fourier form of the Cattaneo–Christov model is more physical because it resolves the problem of the unphysical infinite propagation speed of heat by accounting for finite thermal and solutal relaxation times. The non-Fourier model described by Equations (4) and (5) is now used to develop a new governing system of equations. A magnetic field is applied perpendicularly to the direction of flow. The free-stream condition is considered while taking the constant surface temperature T_w and constant surface concentration C_w into account. The Magnetic Reynolds number is considered to be very small so that induced magnetic field becomes negligible in comparison to the applied magnetic field. The Buongiorno two-phase model is considered since it considers heat and mass transfer processes without neglecting nanoparticle dynamics.

Thus, the mathematical model for radiative magnetohydrodynamic flow of Darcy-Forchheimer Eyring-Powell fluid over a stretching cylinder with convective heating is considered according to the boundary layer theory in relation to the laws of conservation of mass, momentum, and energy. The problem statement is considered based on theoretical considerations and past research. The above problem statement is based on the following assumptions [20, 21]. The governing equations of the mathematical model are formulated in the form of partial differential equations (PDEs) as follows:

$$\frac{\partial(ru)}{\partial x} + \frac{\partial(rv)}{\partial r} = 0. \tag{10}$$

$$\begin{aligned} u\frac{\partial u}{\partial x} + v\frac{\partial u}{\partial r} = \left(\frac{\mu}{\rho}\right)\left(\frac{\partial u^2}{\partial r^2} + \frac{1}{r}\frac{\partial u}{\partial r}\right) + \frac{1}{\rho\beta_c}\left(\frac{\partial u^2}{\partial r^2} + \frac{1}{r}\frac{\partial u}{\partial r}\right) - \frac{1}{6\rho\beta_c^3}\left[\frac{1}{r}(\frac{\partial u}{\partial r})^3 + 3(\frac{\partial u}{\partial r})^2\frac{\partial^2 u}{\partial r^2}\right] \\ -\frac{\sigma B_0^2}{\rho}u - \frac{\mu}{\rho k}u - \frac{F}{\sqrt{k}}u^2. \end{aligned} \tag{11}$$

$$\begin{aligned} u\frac{\partial T}{\partial x} + v\frac{\partial T}{\partial r} = \alpha_f\left(\frac{\partial^2 T}{\partial r^2} + \frac{1}{r}\frac{\partial T}{\partial r}\right) + \Gamma\left[D_m\frac{\partial C}{\partial r}\frac{\partial T}{\partial r} + \frac{D_T}{T_\infty}\left(\frac{\partial T}{\partial r}\right)^2\right] + \lambda_E\left[u^2\frac{\partial^2 T}{\partial x^2} + v^2\frac{\partial^2 T}{\partial r^2}\right. \\ \left. + 2uv\frac{\partial^2 T}{\partial x \partial r} - u\frac{\partial u}{\partial x}\frac{\partial T}{\partial x} - u\frac{\partial v}{\partial x}\frac{\partial T}{\partial r} - v\frac{\partial u}{\partial r}\frac{\partial T}{\partial x} - v\frac{\partial v}{\partial r}\frac{\partial T}{\partial r}\right] + \frac{1}{\rho c_p}\left[(\mu + \frac{1}{\beta c})(\frac{\partial u}{\partial r})^2 - \frac{1}{6\beta c^3}(\frac{\partial u}{\partial r})^4\right] \\ + \frac{\sigma B_0^2}{\rho c_P}u^2 + \frac{\mu}{\rho c_p k}u^2 + \frac{F}{c_p\sqrt{k}}u^3 - \frac{1}{\rho c_p}\frac{\partial qr}{\partial r}. \end{aligned} \tag{12}$$

$$u\frac{\partial C}{\partial x}+v\frac{\partial C}{\partial r}=D_B\left(\frac{\partial^2 C}{\partial r^2}+\frac{1}{r}\frac{\partial C}{\partial r}\right)+\frac{D_T}{T_\infty}\left[\frac{\partial^2 T}{\partial r^2}+\frac{1}{r}\frac{\partial T}{\partial r}\right]+\lambda_C\left[u^2\frac{\partial^2 C}{\partial x^2}+v^2\frac{\partial^2 C}{\partial r^2}+2uv\frac{\partial^2 C}{\partial x\partial r}\right.$$
$$\left.-u\frac{\partial u}{\partial x}\frac{\partial C}{\partial x}-u\frac{\partial v}{\partial x}\frac{\partial C}{\partial r}-v\frac{\partial u}{\partial r}\frac{\partial C}{\partial x}-v\frac{\partial v}{\partial r}\frac{\partial C}{\partial r}\right]-k_r(C-C_\infty). \tag{13}$$

Boundary conditions are expressed as follows:

$$\begin{cases} u=u_w(x)=u_0(\frac{x}{l}), v=0,\ \ k_f\frac{\partial T}{\partial r}=h_f(T_f-T), \\ C=C_w(x)=C_\infty+C_0(\frac{x}{l})\ \ at\ r=R\ and\ u=u_\infty, v=0, T=T_\infty, C=C\infty\ as\ r\to\infty, \end{cases} \tag{14}$$

where c_p is the specific heat at constant pressure, D_T is the thermophoretic diffusion coefficient, D_B is Brownian motion diffusion coefficient, and $\Gamma=\frac{(\rho c_p)_p}{(\rho c_p)_f}$ is the heat capacity ratio, $(\rho c_p)_p$ is the heat capacity of the nanoparticles and $(\rho c_p)_f$ is the heat capacity of the base fluid. q_r is the thermal radiative heat flux, k is the porous media permeability, F is the Forchheimer constant, which is also known as the nonlinear inertial porous resistivity parameter, and k_r is the chemical reaction coefficient. Thermal radiation is the phenomenon of heat energy transfer by means of wave propagation, which can take place in either media or vacuum. It is seen that the radiative heat energy transfer rate is directly proportional to the fourth power of absolute temperature. Using the Rosseland approximation for the radiative heat flux q_r, can write.

$$q_r=\frac{-4\delta^*\partial T^4}{3k^*\partial r}, \tag{15}$$

where the Stefan Boltzmann constant is denoted by $k*$ and the Rosseland mean absorption coefficient by σ^*. Furthermore, the temperature differential in the flow is so small that the Taylor series expansion of T^4 about T_0 yields:

$$T^4=\cong T_0^4+4T^3(T-T_0)+6T_0^2(T-T_0)^2+...$$

Ignoring the terms of the second and higher orders results in:

$$T^4\cong 4T_0^3T-3T_0^4 \text{ so,}$$

$$\frac{\partial T^4}{\partial r}=4T_0^3\frac{\partial T}{\partial r} \tag{16}$$

Using (16) into (15) yields:

$$q_r=\frac{-16\sigma^*T_0^3}{3k^*}\frac{\partial T}{\partial r}$$

Therefore,

$$\frac{\partial q_r}{\partial r}=\frac{-16\sigma^*T_0^3}{3k^*}\left[\frac{\partial^2 T}{\partial r^2}+\frac{1}{r}\frac{\partial T}{\partial r}\right] \tag{17}$$

Substituting (17) into the energy Eq. (12) yields:

$$u\frac{\partial T}{\partial x}+v\frac{\partial T}{\partial r}=\alpha_f\left(\frac{\partial^2 T}{\partial r^2}+\frac{1}{r}\frac{\partial T}{\partial r}\right)+\Gamma\left[D_m\frac{\partial C}{\partial r}\frac{\partial T}{\partial r}+\frac{D_T}{T_\infty}\left(\frac{\partial T}{\partial r}\right)^2\right]+\lambda_E\left[u^2\frac{\partial^2 T}{\partial x^2}+v^2\frac{\partial^2 T}{\partial r^2}+2uv\frac{\partial^2 T}{\partial x\partial r}-\right.$$
$$\left.u\frac{\partial u}{\partial x}\frac{\partial T}{\partial x}-u\frac{\partial v}{\partial x}\frac{\partial T}{\partial r}-v\frac{\partial u}{\partial r}\frac{\partial T}{\partial x}-v\frac{\partial v}{\partial r}\frac{\partial T}{\partial r}\right]+\frac{1}{\rho c_p}\left[\left(\mu+\frac{1}{\beta c}\right)\left(\frac{\partial u}{\partial r}\right)^2-\frac{1}{6\beta c^3}\left(\frac{\partial u}{\partial r}\right)^4\right]+\frac{\sigma B_0^2}{\rho c_p k}u^2 \tag{18}$$
$$+u^2\left(\frac{\mu}{\rho c_p k}+\frac{F}{c_p\sqrt{k}}u\right)+\frac{1}{\rho c_p}\frac{16\sigma^* T_0^3}{3k^*}\left(\frac{\partial^2 T}{\partial r^2}+\frac{1}{r}\frac{\partial T}{\partial r}\right).$$

To transform Equations (10), (11), (12), and (18) into ordinary differential equations (ODEs), the following dimensionless variables are introduced. are introduced.

$$\eta=\left(\frac{r^2-R^2}{2R}\right)\sqrt{\frac{u_o}{vl}},\psi=\sqrt{u_w vl}Rf(\eta),u=u_w f'(\eta),v=-\frac{R}{r}\sqrt{\frac{u_0 v}{l}}f(\eta),$$
$$\theta=\frac{T-T_\infty}{T_f-T_\infty},\Phi(\eta)=\frac{C-C_\infty}{C_w-C_\infty}. \tag{19}$$

Equations (10), (11), (12), and (18) are transformed into ordinary differential equations (ODEs). Equation (10) is automatically satisfied when the similarity transformations (19) are applied, while Equations (11), (12), and (18) are reduced to the following ODEs:

$$(1+\delta)(1+2\gamma\eta)f'''+ff''-(f')^2+2\gamma(1+\delta)f''-\frac{4}{3}\delta\lambda\gamma(1+2\gamma\eta)(f'')^3-\delta\lambda(1+2\gamma\eta)^2 f'''(f'')^2$$
$$-Mf'-Daf'-(1+F)(f')^2=0. \tag{20}$$

$$\frac{(1+2\gamma\eta)(1+Rd)}{Pr}\theta''+\frac{2\gamma(1+Rd)}{Pr}\theta'-\lambda_t\left(f^2\theta''+ff'\theta'\right)+f\theta'+Nb(1+2\gamma\eta)\theta'\phi'+Nt(1+2\gamma\eta)(\theta')^2+$$
$$Ec(f'')^2\left[(1+\delta)(1+2\gamma\eta)-\frac{1}{3}\delta\lambda(f'')^2\right]+Ec\,(M+Da)\,(f')^2+EcF(f')^3=0. \tag{21}$$

$$(1+2\gamma\eta)\phi''+2\gamma\phi'+Scf\phi'$$
$$-Sc\lambda_c\left(f^2\phi''+ff'\phi'+\frac{Nt}{Nb}\left[(1+2\gamma\eta)\theta''+2\gamma\theta'\right]\right)-\alpha\phi=0. \tag{22}$$

In Eqs. (20)–(22), the dimensionless parameters are defined as follows:

$\delta=\frac{1}{\mu\beta_c}$ is Eyring-Powell fluid parameter, $\gamma=\frac{1}{R}\sqrt{\frac{\nu l}{u_o}}$ is cylinder curvature parameter, $\lambda=\frac{u_0^3 x^2}{2c^2 l^3\nu}$ is a fluid parameters, M = $\frac{\sigma B_0 l}{\rho u_0 l}$ is magnetic parameter, Pr = $\frac{\nu}{\alpha_f}$ is Prandtl number, $\lambda_t=\frac{\lambda_E u_o}{l}$ is thermal relaxation time parameter. Da = $\frac{\rho K u_0}{\mu l}$ is the Darcy number, K=$\frac{\mu l}{u_o\rho k_o}$ is a porous parameter, F=$\frac{F}{\sqrt{k}}$ Forchheimer parameter, Nb =$\frac{\Gamma D_B(C_w-C_\infty)}{\nu}$ is the Brownian motion parameter, Nt = $\frac{\Gamma D_T(T_w-T_\infty)}{\nu T_\infty}$ is the thermophoresis parameter, Sc=$\frac{\nu}{D_B}$ is the Schmidt number, λ_c = $\frac{\lambda_C u_o}{l}$ is the solutal relaxation time parameter, Ec = $\frac{u_0^2}{c_p(T_w-T_\infty)}$ is the Eckert number(or viscous dissipation parameter), Rd=$\frac{16\sigma^* T_\infty^3}{3k^*\rho c_p}$ is radiation parameter, and $\alpha=\frac{k_r}{\nu}$ is chemical reaction parameter.

The converter boundary conditions in (14) by using similarity transformation become:

$$f(0)=0,f'(0)=1,\theta'(0)=-Bi(1-\theta(0)),\phi(0)=1,$$
$$f'(\infty)=A,\ \ \theta(\infty)=0,\ \ \phi(\infty)=0. \tag{23}$$

Where, $Bi = \frac{h_f}{k_f}\sqrt{\frac{vl}{u_0}}$ is Biot number of cylinder's, and A=$\frac{u_\infty}{u_w}$ is velocity ratio parameter. Using your similarity variables, we first write the temperature in non-dimensional form:

$$\theta = \frac{T - T_\infty}{T_f - T_\infty} \tag{24}$$

implies

$$T = T_\infty + (T_f - T_\infty)\theta(\eta). \tag{25}$$

Hence,

$$\frac{\partial T}{\partial r} = (T_f - T_\infty)\frac{\partial \theta}{\partial \eta}\frac{\partial \eta}{\partial r} \tag{26}$$

. From your similarity variable,

$$\eta = \left(\frac{r^2 - R^2}{2R}\right)\sqrt{\frac{u_0}{\nu l}}, \quad \frac{d\eta}{dr} = \frac{r}{R}\sqrt{\frac{u_0}{\nu l}}. \tag{27}$$

Now substitute Eqs.(26) and (27) into convective boundary the given heat balance equation:

$$k_f \frac{\partial T}{\partial r} = h_f(T_w - T). \tag{28}$$

becomes:

$$k_f(T_f - T_\infty)\frac{d\theta}{d\eta}\frac{r}{R}\sqrt{\frac{u_0}{\nu l}} = h_f(T_f - T_\infty)(1 - \theta). \tag{29}$$

Both side divided by

$$(T_f - T_\infty) \tag{30}$$

,
we get

$$.k_f \frac{d\theta}{d\eta}\frac{r}{R}\sqrt{\frac{u_0}{vl}} = h_f(1 - \theta) \tag{31}$$

.
At the boundary r=R, and $\eta = 0$).

$$k_f\sqrt{\frac{u_0}{vl}}\theta'(0) = h_f(1 - \theta(0)) \implies \theta'(0) = \frac{h_f}{k_f}\sqrt{\frac{vl}{u_0}}(1 - \theta()0) \tag{32}$$

. Where $Bi = \frac{h_f}{k_f}\sqrt{\frac{vl}{u_0}}$ is Biot number of cylinder's.

Therefore, the convective boundary non-dimensional is written

$$\theta'(0) = Bi(1 - \theta(0)). \tag{33}$$

The three basic quantities that are of great importance in understanding the practical applications of industrial engineering are skin friction coefficient, heat transfer, and mass transfer rates. In this research work, skin friction

coefficient, local Nusselt number, and Sherwood number have been taken into account.The skin friction coefficient, commonly known as wall shear stress, is denoted by (C_f).

$$Cf_x = \frac{2\tau_w}{u_w^2} \tag{34}$$

The shear stress τ_{ij} of the Eyring-Powell fluid at r=R (or wall shear stress) may be found using:

$$\tau_w = [\tau_{ij}]_{r=R} = \left[\mu\frac{\partial u}{\partial r} + \frac{1}{\beta c}\frac{\partial u}{\partial r} - \frac{1}{6\beta c^3}(\frac{\partial u}{\partial r})^3\right]_{r=R}$$

Thus, the dimensionless form of the skin friction coefficient $C_f$in (34) is as follows

$$\frac{1}{2}C_f\sqrt{Re_x} = (1+\delta)f''(0) - \frac{1}{3}E\lambda f''(0)^3 \tag{35}$$

, The wall heat transfer rate, or local Nusselt number (Nu), is defined as follows:

$$Nu_x = \frac{xq_w}{k(T_w - T_\infty)} \tag{36}$$

where $q_w = -k(\frac{\partial T}{\partial r})_{r=R}$ is the heat flux at the surface of the cylinder. Thus, the dimensionless local Nusselt number is given by:

$$\frac{Nu_x}{\sqrt{Re_x}} = -(1+Rd)\theta'(0) \tag{37}$$

, and also, the mass transfer rate at the surface, or local Sherwood number (Sh), is defined as follows:

$$Sh_x = \frac{xJ_w}{D_B(C_w - C_\infty)} \tag{38}$$

where the mass flux at the surface is $J_w = D_B(\frac{\partial C}{\partial r})_{r=R}$. Thus, the dimensionless local Sherwood number can be expressed as follows:

$$\frac{Sh_x}{\sqrt{Re_x}} = -\phi'(0) \tag{39}$$

,where $Re_x^{\frac{1}{2}} = \sqrt{\frac{u_0 xR}{l\nu}}$.

3 Numerical Solutions

To assess the effectiveness and validity of the proposed framework, some illustrative examples have been considered in the next section. The solutions of the Homotopy Analysis Method (HAM) have been used as benchmark simulations. The nonlinear Equations (11), (12), and (18), along with the boundary conditions in Eq. (23), constitute a strongly coupled system. It is obtained through the solution of this system using the Homotopy Analysis Method (HAM), which is a very efficient and reliable analytical method. Employed HAM for solving nonlinear differential equations under strongly and weakly nonlinear conditions [22]. This method makes it possible to avoid discretization and restrictive assumptions, which makes it universal, efficient, and devoid of rounding errors. HAM technique is a combination of the advantages of numerical and analytical methods. Hence, it is popular among many researchers in science, engineering, and finance, who use this method for solving nonlinear problems. In our research, we will be using BVPh2.0, which is a package in Mathematica that applies HAM and is in line with previous research [23, 24]. This package was successfully used in solving many problems concerning non-Newtonian fluid flows.

The Homotopy Analysis Method (HAM) is a semi-analytical method, that can be used to solve nonlinear differential equations. The procedure usually consists of the following steps:
Step 1:Consider the nonlinear differential equation;

$$N[u(\eta)] = 0. \tag{40}$$

where N is a nonlinear operator $u(\eta)$ are the unknown function. Boundary conditions

$$B(u, \frac{du}{d\eta}, ...) = 0. \tag{41}$$

Step 2: Choose Initial Guesses
The initial guesses are chosen such that they satisfy the boundary conditions given in Eq. (23). For a system of equations, choose $f_0(\eta)$, $\theta_0(\eta)$, $\phi_0(\eta)$ such that all boundary conditions are satisfied.

A suitable initial guess for the velocity profile that satisfies the prescribed boundary conditions is given by

$$f_0(\eta) = A\eta + (1-A)(1-e^{-\eta}). \tag{42}$$

In the same way, to fulfill the convective thermal boundary condition, an initial guess is considered as

$$\theta_0(\eta) = Ce^{-\eta} \tag{43}$$

with C being the constant.

Boundary condition for temperature at wall

$$\theta_0(0) = C. \tag{44}$$

It derivative

$$\theta_0'(0) = -C. \tag{45}$$

Substituting Eq. (45) and (44) into the With the help of the convective boundary condition described in Eq. (2), we have

$$-C = -Bi(1-C), \tag{46}$$

we get

$$C = \frac{Bi}{1+Bi}. \tag{47}$$

In that case, the initial temperature guess can be given by

$$\theta_0(\eta) = \frac{Bi}{1+Bi}e^{-\eta}. \tag{48}$$

that satisfies the boundary condition for convection. In the same way, the initial guess satisfying the boundary conditions for concentration is chosen to be

$$\phi_0(\eta) = e^{-\eta}. \tag{49}$$

Thus, Eq (50) and the boundary conditions along with Eq.(51) for their respective initial guesses can be

$$\begin{aligned} f(0)=0, \qquad f'(0)=1, \qquad f'(\infty)=A, \\ \theta'(0)=-Bi\,(1-\theta(0)), \qquad \theta(\infty)=0, \\ \phi(0)=1, \qquad \phi(\infty)=0. \end{aligned} \tag{50}$$

$$\begin{aligned} f_0(\eta) &= A\eta+(1-A)(1-e^{-\eta}), \\ \theta_0(\eta) &= \frac{Bi}{1+Bi}e^{-\eta}, \\ \phi_0(\eta) &= e^{-\eta}. \end{aligned} \tag{51}$$

Step 3: Define Linear Operators.

$$\begin{aligned} \mathcal{L}_f[f(\eta)] &= f'''(\eta)-f(\eta), \\ \mathcal{L}_\theta[\theta(\eta)] &= \theta''(\eta)-\theta(\eta), \\ \mathcal{L}_\phi[\phi(\eta)] &= \phi''(\eta)-\phi(\eta). \end{aligned} \tag{52}$$

Step 4: Construction of Nonlinear Operators

Under the Homotopy Analysis Method (HAM), the nonlinear operators that correspond to the dimensionless momentum, energy, and concentration equations can be expressed as:

$$\begin{cases} N_f[f(\eta)]=0, \\ N_\theta[\theta(\eta)]=0, \\ N_\phi[\phi(\eta)]=0. \end{cases} \tag{53}$$

Step 5: Zeroth-Order Deformation Equations

Introduce embedding parameter p∈[0,1]:

$$(1-p)\mathcal{L}_f[f(\eta,p)-f_0(\eta)] = ph_fN_f(\eta,p), \tag{54}$$
$$(1-p)\mathcal{L}_\theta[\theta(\eta,p)-\theta_0(\eta)] = ph_\theta N_\theta(\eta,p), \tag{55}$$
$$(1-p)\mathcal{L}_\phi[\phi(\eta,p)-\phi_0(\eta)] = ph_\phi N_\phi(\eta,p). \tag{56}$$

Where, h_f, h_θ, h_ϕ are convergence-control parameters.

Step 6: m-th Order Deformation Equations.

Differentiate with respect p, set p=0:

$$\mathcal{L}_f[f_m-\chi_m f_{m-1}] = h_fR_{f,m}, \tag{57}$$
$$\mathcal{L}_\theta[\theta_m-\chi_m\theta_{m-1}] = h_\theta R_{\theta,m}, \tag{58}$$
$$\mathcal{L}_\phi[\phi_m-\chi_m\phi_{m-1}] = h_\phi R_{\phi,m}. \tag{59}$$

Where:

$$\chi_m=\begin{cases} 0, & m\le 1, \\ 1, & m>1. \end{cases} \tag{60}$$

and R_i,n(η)are the nonlinear residuals determined from previous-order solutions.

Step 7: Boundary Conditions for Each Order.

The corresponding boundary conditions for the mth-order deformation equations are given by

$$\begin{aligned} &f(0)=0, \quad f'(0)=0, \quad f'(\infty)=A, \\ &\theta'(0)=-Bi(1-\theta(0)), \quad \theta(\infty)=0, \\ &\phi(0)=0, \quad \phi(\infty)=0. \end{aligned} \tag{61}$$

Step 8: Construction of the HAM series solution.
After selecting suitable values of h_i, the truncated HAM series solutions are constructed up to a finite order N:

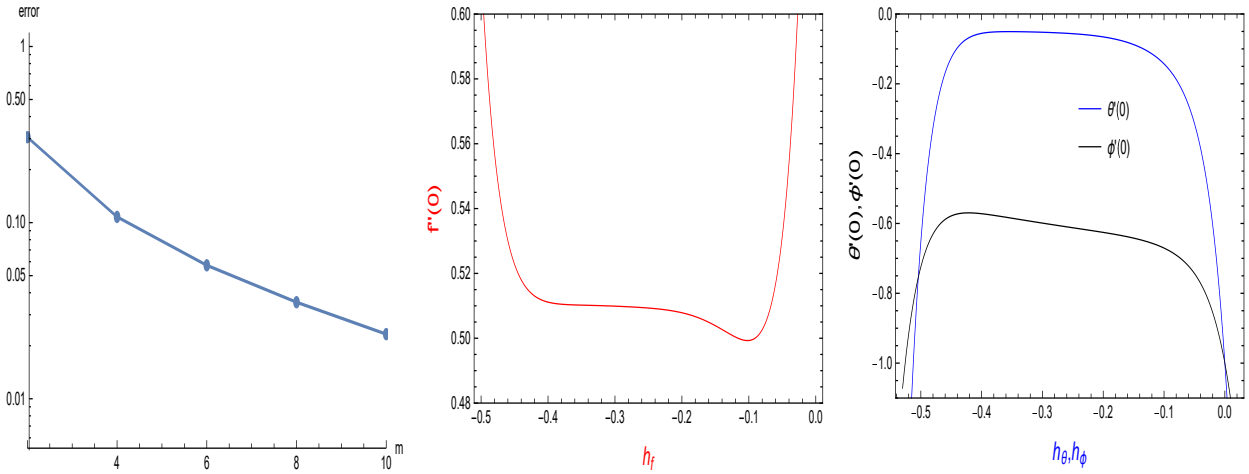
$$f(\eta)=f_0(\eta)+\sum_{m=1}^{\infty} f_m(\eta), \tag{62}$$

$$\theta(\eta)=\theta_0(\eta)+\sum_{m=1}^{\infty} f_m(\eta), \tag{63}$$

$$\phi_(\eta)=\phi_0(\eta)+\sum_{m=1}^{\infty} f_m(\eta). \tag{64}$$

Step 9: Convergence Control We must plot h-curves for: f"(0) vs h_f, $\theta'(0)$ vs h_θ, and $\phi'(0)$vs h_ϕ.
Step 10: Verification and Physical Interpretation: The solutions from the HAM are verified by comparison to numerical results that are newly available in published literature.

We have used the Homotopy Analysis Method (HAM) to get the analytical solution of the nonlinear ODEs representing our situation.



(a) (b) (c)

Fig. 2 The graphical depictions of (a) the total Squared Residual Errors against order of HAM approximations, (b) h- curve for f"(0), (c) h- curves for $\theta'(0)$ and $\phi'(0)$.

It can be clearly seen from Fig.2a that the error dramatically drops with the increase in the number of couples. The convergence of the algorithm when solving the problem of flow is therefore guaranteed. The correctness of the results can also be proven by comparing the results obtained in this work with the results of some other works on similar problems. The convergence of the algorithm and the agreement of the results with some other papers are therefore proved.The convergence region is quite significant for obtaining series solutions. This is because series solutions provide a convergence region, which means several choices can be made concerning the value of the convergence control parameter h. Therefore, from Fig. (2b-2c), the convergence of the HAM solution of the velocity field through the (h_f)-curve of (f"(0)) is depicted. From the outcomes, a wide horizontal line in the region ($-0.42 \leq h_f \leq 0.08$) is

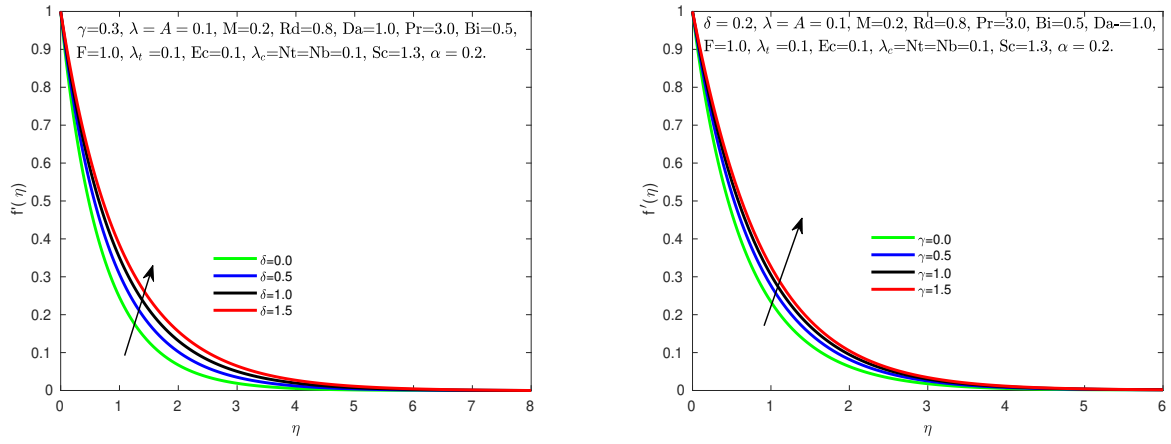
depicted. This type of pattern shows that the series solution is independent of the value of the convergence control parameter h, hence convergent. Therefore, the region of validity of (h_f) shall be $(-0.42 \leq h_f \leq 0.08)$. The value of $(h_f = -0.30)$ will be used throughout the analysis, as it falls within the convergence region. The values of (h_θ) and (h_ϕ) are chosen to be -0.47 $\leq h_\theta \leq$0.06 and -0.45$\leq h_\phi \leq$-0.07, respectively. The differential system is solved numerically using the Mathematica program.

4 Results and Discussion

This system of nonlinear ordinary differential equations (20)-(22) along with the corresponding boundary conditions (23) is solved by using the optimal HAM. Results for the velocity profile, temperature profile, and concentration profile are discussed through graphs for some values of the governing parameters. Comparison of flow characteristics over a stretched cylinder is made through tables.

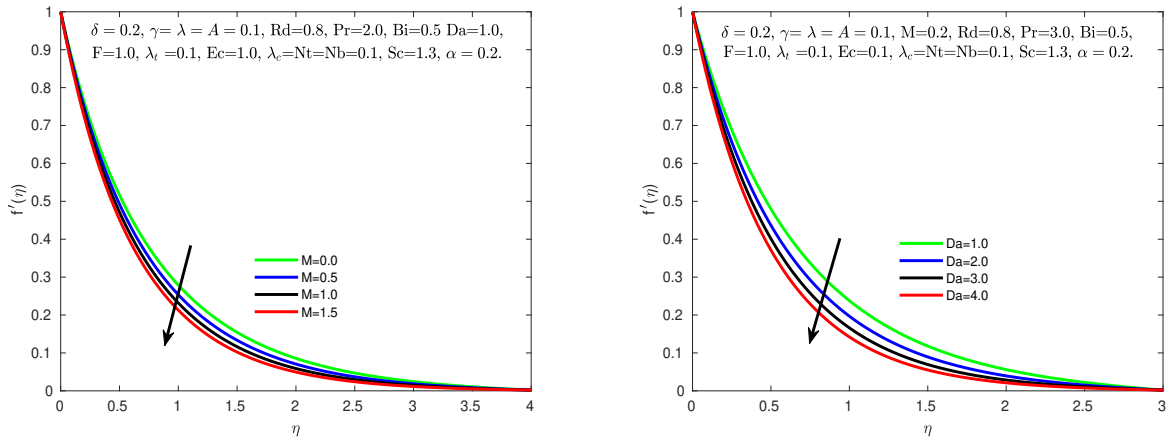
4.1 The Velocity Profiles

Figures 3–5 show the velocity profiles for different values of the governing parameters, namely the Eyring–Powell fluid parameter (δ), curvature parameter (γ), velocity ratio parameter A, Magnetic parameter parameter(M), Darcy number (Da), and Forchheimer number (F), on the velocity profile $f'(\eta)$ of the Eyring–Powell nanofluid flow.



(a) (b)

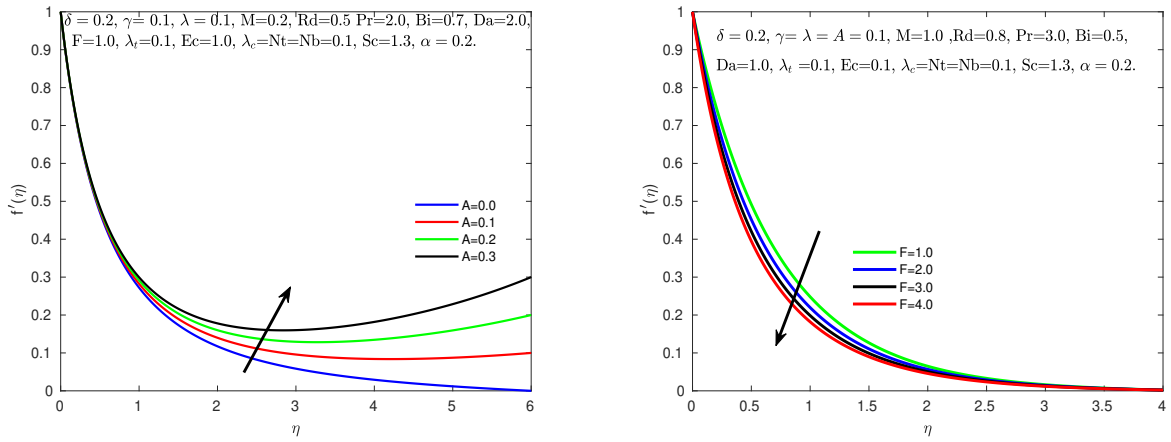
Fig. 3 Effects of *(a)* Eyring–Powell fluid parameter (δ) and *(b)* curvature parameter (γ) on the velocity profile $f'(\eta)$.



(a) (b)

Fig. 4 Effect of *(a)* magnetic parameter (M) and *(b)* Darcy number (Da) on the velocity profile.

Fig.3a depicts the impact of the Eyring-Powell fluid parameter (δ) on the velocity profile. It can be seen that as the value of δ is increased, there is a large increase in the velocity of the fluid in the boundary layer. This is because when the value of δ increases, the viscosity of the fluid decreases under shear conditions. Since the Eyring-Powell fluid model is a shear-thinning fluid, increasing the value of δ will lead to a decrease in the viscosity of the fluid. The result is that since the viscous force has reduced, the fluid accelerates, which increases its velocity. However, Fig.3b shows that the effect of the cylinder curvature parameter (γ) is to affect the geometry of the flow field. When the value of the parameter γ is increased, it leads to an increase in the curvature effects in the flow field. This leads to a modification of the momentum distribution in the radial direction, resulting in an increase in the momentum boundary layer thickness due to an increase in the momentum diffusion effect. Fig.4a represents the impact of the magnetic parameter (M) on the velocity profile. This can be explained physically by the fact that the existence of the magnetic field gives rise to the Lorentz forces that resist the fluid flow by acting against its motion and reducing its velocity. As the magnetic parameter value increases, the Lorentz forces become stronger, thereby increasing the resistance force on the fluid flow. Thus, the fluid flow becomes slow, causing a reduction in its velocity. Fig.4b represents the impact of the Darcy number (Da) on the velocity profile. From Figure 4b, it can be seen that with an increase in the Darcy number, there is a reduction in the fluid velocity in the boundary layer. It is common knowledge that the Darcy number has to do with the permeability of the porous medium. However, in this problem, an increase in Da means increased fluid-porous matrix interactions.



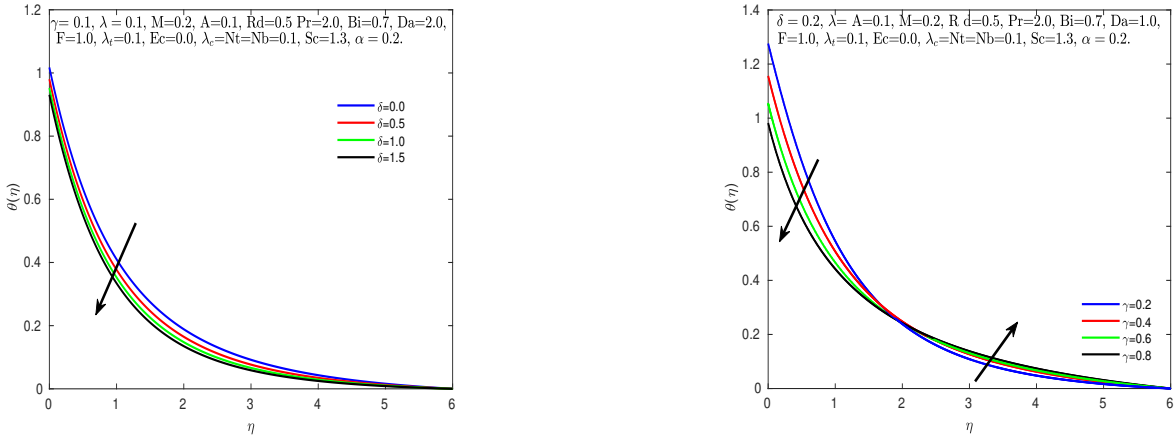
(a) (b)

Fig. 5 Effects of *(a)* velocity ratio parameter (A) and *(b)* Forchheimer parameter (F) on the velocity profile $f'(\eta)$.

From Fig. 5a, it can be seen that the velocity profile in the boundary layer increases as the velocity ratio parameter A increases. The velocity ratio parameter is the ratio of the surface stretching velocity (u_w) to the free-stream velocity (u_∞). Mathematically, when A takes high values, it implies that the surface stretches faster than the surrounding fluid flow. This makes the momentum transfer between the surface and the fluid better, hence forming a thick hydrodynamic boundary layer with higher fluid velocities. Thus, an increase in A results in a high velocity profile. Fig. 5b, on the other hand,d shows the effect of the Forchheimer parameter. The Forchheimer parameter is used to represent the inertial resistance of the porous medium. It is due to the additional non-linear drag force in the porous structure, which acts against the fluid flow. When F increases, the inertial resistance becomes high, making the momentum transfer in the boundary layer poor. Hence,ce the fluid flow faces more resistance, thus reducing the velocity.

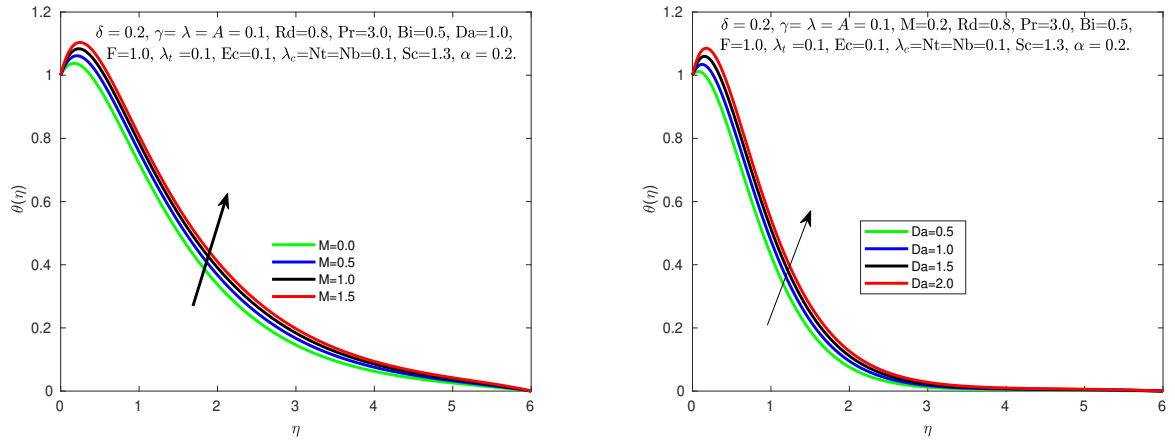
4.2 Temperature Profiles

In the case of the nonlinear ordinary differential equation system (21) under the above-mentioned boundary conditions in Eq. (23), the optimal HAM approach is used to solve the energy equation. Figs. 6-11 show the impacts of different embedding parameters such as the Eyring-Powell fluid parameter, curvature parameter, Forchheimer parameter, magnetic parameter, thermal radiation parameter, thermophoresis parameter, Eckert number, Darcy number, Biot number, thermal relaxation time, Brownian motion parameter, and Prandtl number, on the temperature distribution and thermal boundary layer thickness.



(a) (b)

Fig. 6 Effect of *(a)* the Eyring–Powell fluid parameter (δ) and *(b)* the cylinder curvature parameter (γ) on the temperature profile.

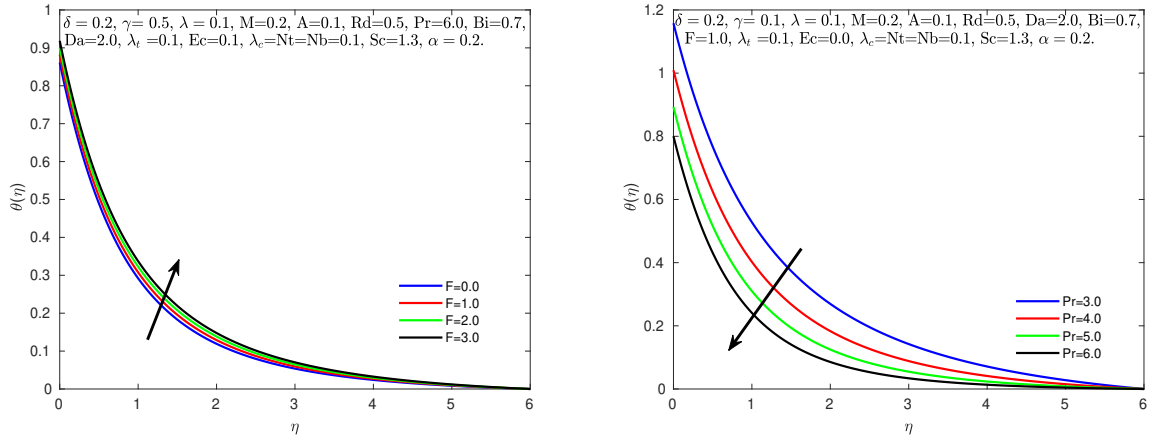


(a) (b)

Fig. 7 Effect of *(a)* Magnetic parameter (*M*) and *(b)* Darcy number (Da) on the temperature profile .

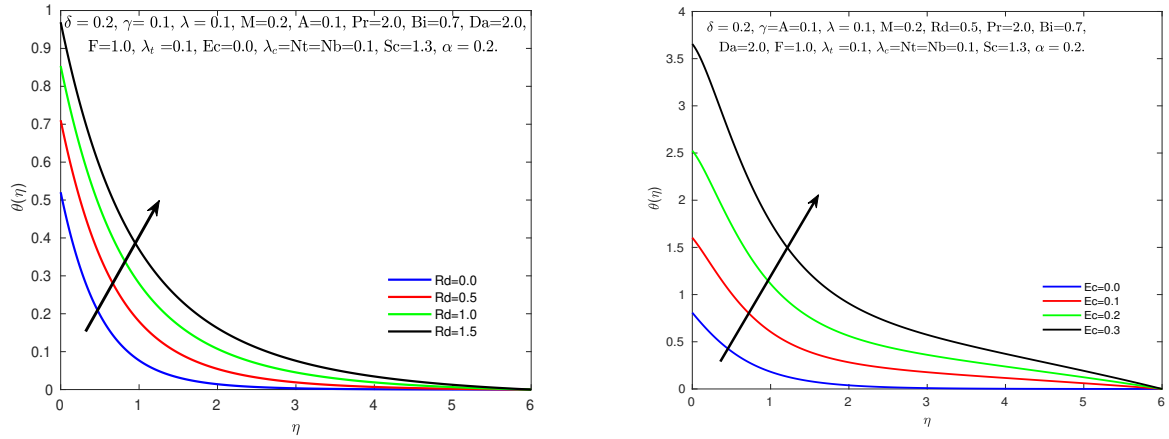
As can be seen in Fig. 6a, the fluid model of Eyring-Powell possesses shear-thinning and shear-thickening properties as a non-Newtonian fluid, whereby viscosity is a function of the strain rate. The temperature profile decreases in the thermal boundary layer with an increase in the value of the Eyring-Powell parameter δ. An increase in the value of the Eyring-Powell parameter δ decreases the fluid viscosity, thus facilitating the reduction in momentum diffusivity and therefore flow resistance. As a result, the convective heat transfer process is increased due to the fluid particle motion in the direction of the wall. Thus, the temperature profile decreases in the thermal boundary layer. Moreover, an increase in the value of the Eyring-Powell parameter δ increases the shear-thinning properties of the fluid, whereby its viscosity decreases with an increase in shear rate, and hence increases thermal energy transfer from the wall to the free stream.Fig.6b reveals the impact of the curvature parameter γ on the temperature distribution θ(η). With the increase in the value of γ, the radius of the cylinder decreases, and consequently, the time for the fluid to stay close to the surface becomes smaller, leading to improved heat transfer. This results in a decrease in the temperature distribution close to the cylinder surface. It is also noted that the temperature distribution in the case of the flat plate is greater than that of the cylindrical surface.

From Fig.7a, it can be observed that both temperature profiles $\theta(\eta)$ and $theta(\ eta)$ are greater as there is an increase in the value of the magnetic parameter M. As the value of M increases, then there is also an increase in the value of the Lorentz force, which resists the motion to develop more thermal energy because of increased flow resistance, increasing the temperature. From Fig.7b, it can be observed that there is an increase in the temperature distribution in the flow regime as there is an increase in the Darcy number (Da). The increase in the value of Da represents the increase in the permeability of the porous medium, which results in the reduction of resistance to fluid flow in the porous medium. That is, there is an improvement in convective transport of thermal energy due to easy flow of fluid in the porous medium. Additionally, there is a reduction in the dampening effect of the solid on the fluid flow in the porous medium due to high permeability of the porous medium, meaning that the drag force reduces.



(a) (b)

Fig. 8 Effect of *(a)* Forchheimer parameter(F) and *(b)* Prandtl number (Pr) on the flow temperature profile.



(a) (b)

Fig. 9 Effect of *(a)* radiation parameter (*Rd*) and *(b)* Eckert number (*Ec*) on the temperature profile.

As shown in Fig. 8a, there is an inverse relation between the temperature distribution and the Forchheimer parameter (F). In other words, for a higher Forchheimer parameter, the temperature profile decreases near the sheet surface

due to increased inertial resistance caused by the porous medium and results in reduced velocity and an increase in the thermal field within the boundary layer. The effect of Prandtl number on the temperature distribution is investigated and discussed in Fig. 8b. It can be seen from the figure that for higher values of the Prandtl number, there will be a lower temperature distribution and thermal boundary layer thickness due to lower thermal diffusivity compared to momentum diffusivity.

Fig.9a depicts the impact of the radiation parameter(Rd) on the temperature profile. It is seen from the above figure that as Rd increases, the temperature and the thickness of the thermal boundary layer also increase. This happens because higher values of the radiation parameter result in a greater amount of energy transportation in the fluid, thus increasing the temperature profile. Fig.9b shows the temperature profile, which is dependent on the viscous dissipation parameter(Ec), otherwise known as the Eckert number(Ec). With the increase in Ec, there is an increase in the temperature field.

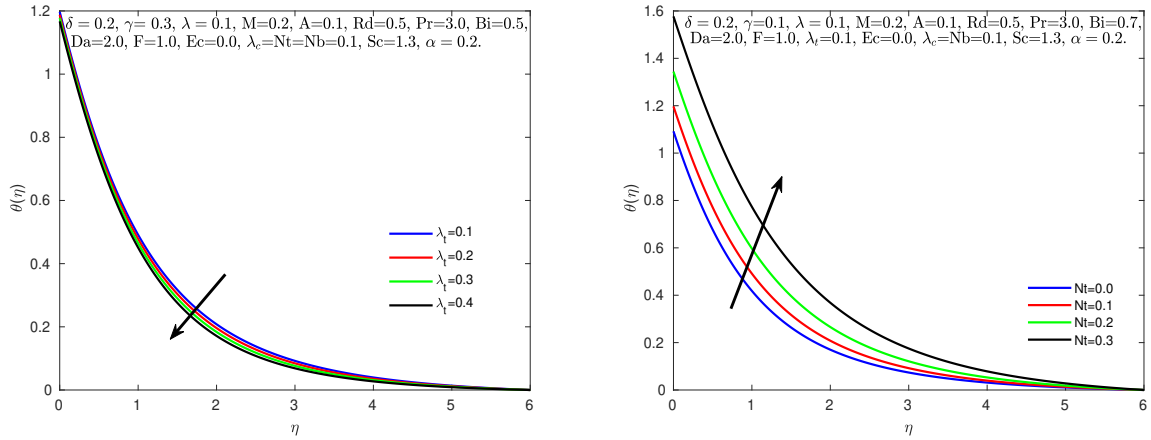


Fig. 10 Effect of *(a)*thermal relaxation time parameter (λ_t) and *(b)*thermophoresis parameter(Nt) on flow temperature profile.

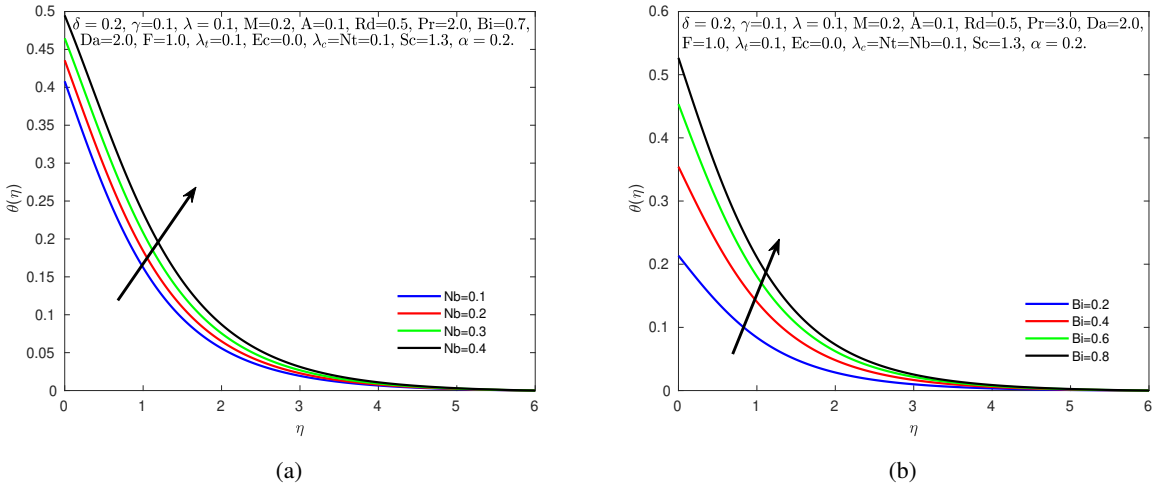


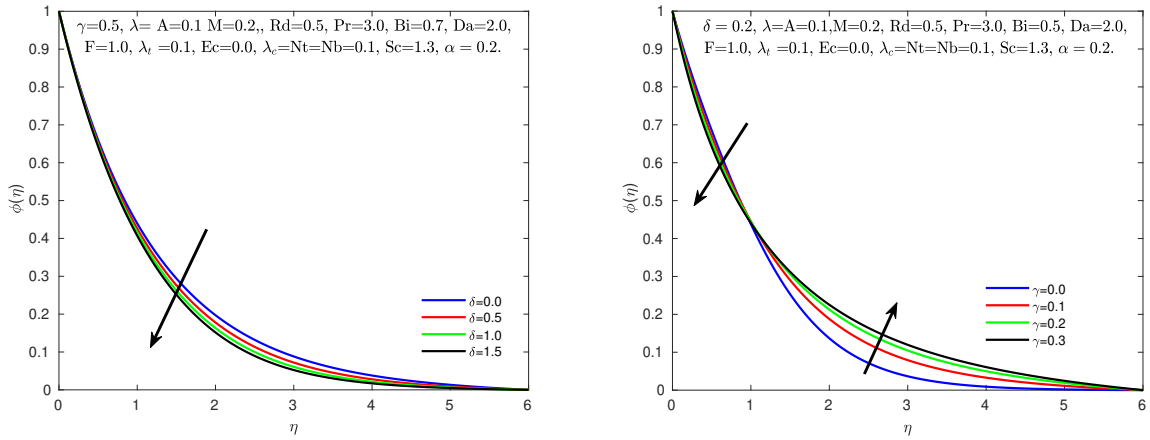
Fig. 11 Effect of *(a)*Brownian motion parameter (Nb) and *(b)* Biot number (Bi) on the flow temperature profile.

Fig.10a shows that thermal boundary layer thickness and temperature profile depend on the thermal relaxation time parameter λ_t. An increase in λ_t leads to a reduction in the temperature profile. The increase in thermal relaxation time means that the nanofluid needs a longer period to react to the change in temperatures, reducing the heat transfer process between the medium and causing a decrease in temperature profile. If λ_t decreases, then the fluid will respond faster to changes in temperature, thus resulting in high temperature levels. It can be noted that when λ_t=0, then the Fourier heat conduction equation reduces to the classical Fourier law of heat conduction. As such, the Fourier law of heat conduction is applicable in explaining the heat conduction process that occurs at much faster rates than the non-Fourier heat flux law. Fig.10b indicates how the thermophoresis parameter(Nt) affects the temperature profile ($\theta(\eta)$). Thermophoresis is a phenomenon whereby the suspended nanoparticles move from one place to another. It is seen that an increase in Nt affects both the temperature profile and thermal boundary layer thickness.

From Fig. 11a, it is seen that the temperature profiles and thermal boundary layer thickness have an increment with an increase in the Brownian motion parameter (Nb). Brownian motion represents the erratic motion of the nanoparticles dispersed in the base fluid because of molecular collisions. An increase in the Brownian motion parameter signifies that the intensity of the nanoparticle motion has been increased, resulting in an increased diffusion of energy within the fluid. Hence, this makes the temperature field and the thickness of the thermal boundary layer increase. Fig. 11b demonstrates the influence of Biot number (Bi) on the temperature profiles. It is clear from the figure that the temperature profiles have increased with the increment in Bi numbers. This means that when the value of the Biot number is high, the convection heat transfer will be enhanced at the boundary, thus enhancing the heat exchange between the surface and the fluid. This results in increased thickness of the thermal boundary layer.

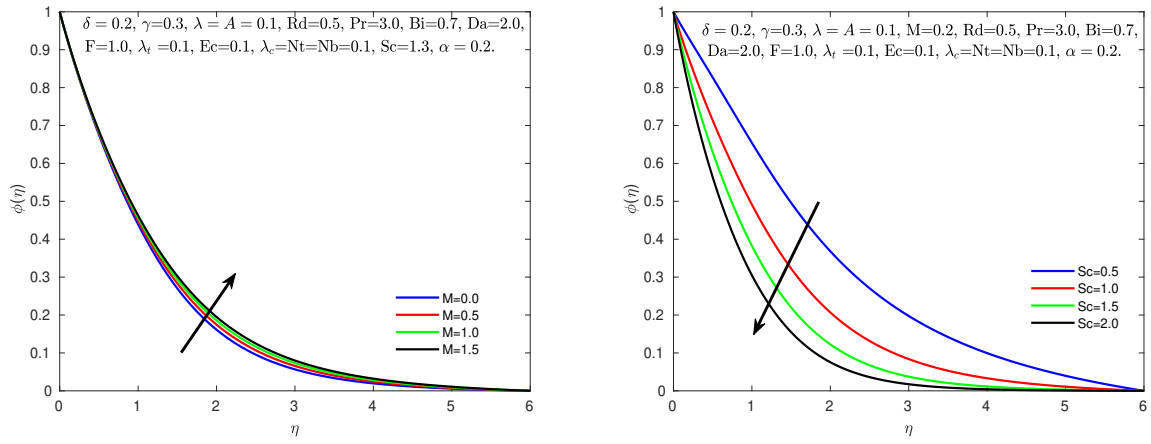
4.3 Concentration Profiles

Figures 12–14 demonstrates that the effects of various embedded parameters, including the Eyring–Powell fluid parameter, curvature parameter, magnetic parameter, Schmidt number, solutal relaxation parameter, Brownian motion parameter, and chemical reaction parameter, on the concentration field $\phi(\eta)$ and the corresponding solutal (species) boundary layer thickness.



(a) (b)

Fig. 12 Effect of *(a)* Eyring-Powell fluid parameter (δ) and *(b)* cylinder curvature parameter(γ) on the flow concentration profile.

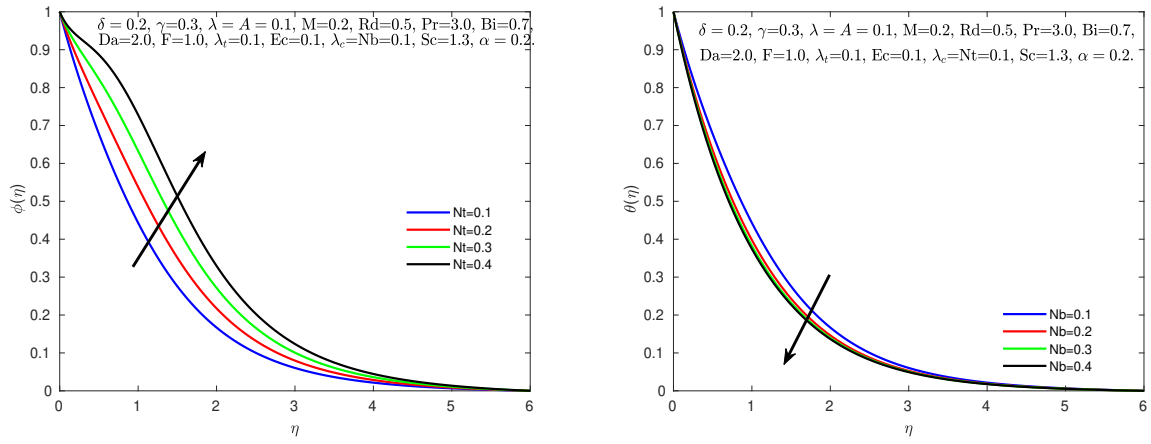


(a) (b)

Fig. 13 Effect of *(a)* Magnetic parameter(*M*), and *(b)* Schmidt number (Sc) on the flow concentration profile.

Fig.12a shows how the rise in the value of the Eyring-Powell fluid parameter (δ) increases the non-Newtonian nature of the fluid by reducing its viscosity, and hence the concentration boundary layer becomes thin. This makes the mass diffusion low, and this decreases the concentration profile. In Fig. 12b, one can see how the curvature parameter (γ) influences the mass transfer properties of the Eyring-Powell fluid flow over a stretching cylinder. The increase in the curvature parameter causes an increase in the velocity gradient near the wall and consequently the accumulation of solute near the wall, which increases the concentration profile. But far away from the wall, the concentration profile decreases because of the strong convective transport due to the curvature parameter.

Fig.13a shows the influence of the magnetic parameter (M) on the concentration profile. The magnetic parameter (M) denotes the intensity of the applied transverse magnetic field to the electrically conducting fluid. The concentration profile in the boundary layer increases with the increase in M. The physical explanation for this is that the application of a magnetic field produces the Lorentz force that resists the flow of the fluid and acts as a resistive force. The convective mass transfer in the direction of the flow will be hindered. The decrease in the velocity of the fluid makes diffusion more favorable than convection and hence makes it possible to have a high concentration of species in the boundary layer. Fig.13b shows the inverse influence of the Schmidt number (Sc) on the concentration profile $\phi(\eta)$. It can be observed that as the value of the Schmidt number increases, there is a decrease in the concentration profile $\phi(\eta)$. This happens because the Schmidt number is the ratio of momentum diffusivity to mass diffusivity; hence, the larger the Schmidt number, the smaller the mass diffusivity.



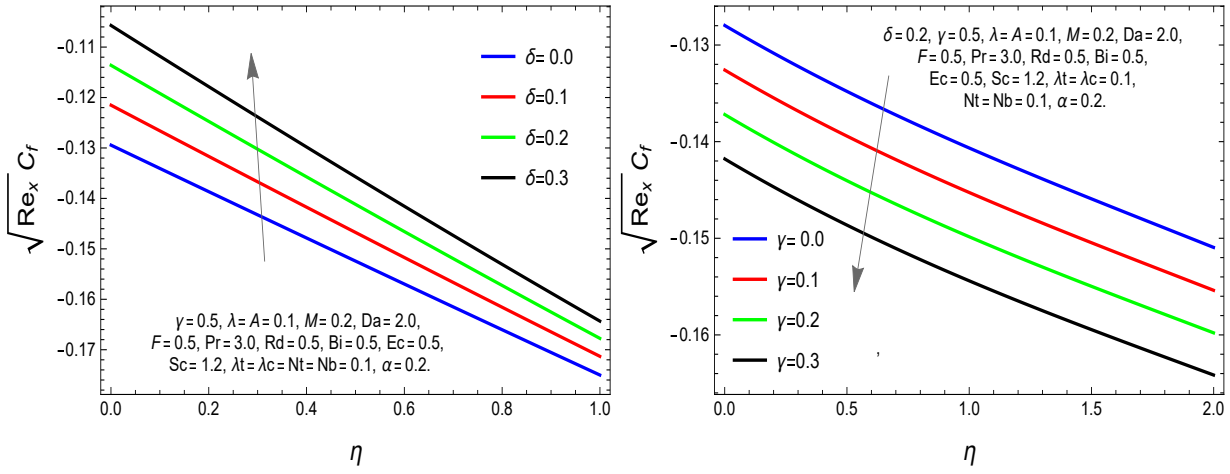
(a) (b)

Fig. 14 Effect of *(a)* thermophoresis parameter(Nt), and *(b)* Brownian motion parameter (Nb)on the flow concentration profile.

Fig.14a shows the impact of changes in the value of the thermophoresis parameter (Nt) on the concentration profile. An increase in the value of Nt implies an increase in the number of particle movement from the heated surface to the fluid. This implies that the concentration profile is higher. Fig.14b represents the impact of changes in the value of the Brownian motion parameter (Nb) on the concentration profile. This results from the randomness of Brownian motion, which distributes particles uniformly in the concentration profile.

4.4 Effects of Changes of Parameters on the Skin Friction, Local Nusselt Number, and Local Sherwood Number Profiles

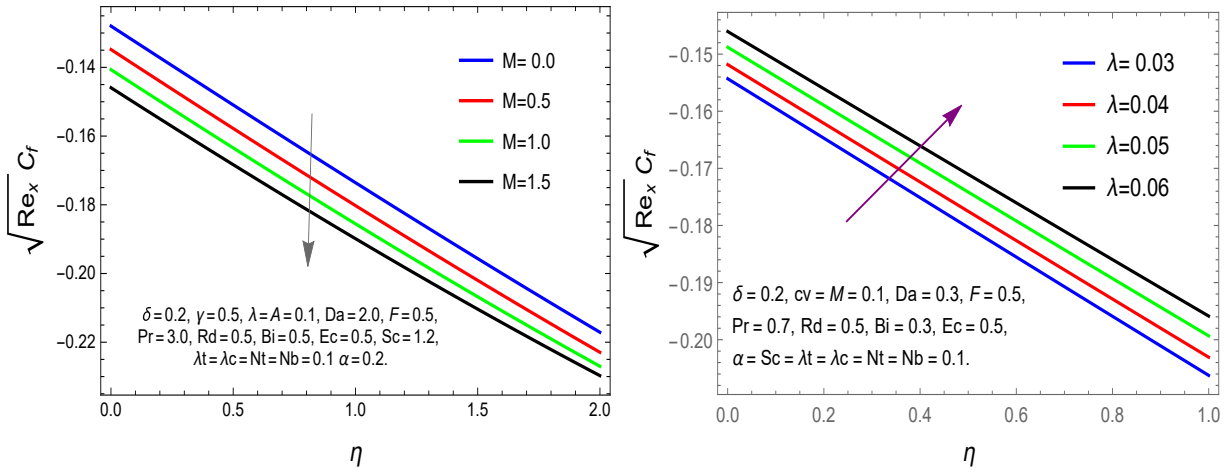
Figs. 15-22 show the effect of various control parameters on the skin friction coefficient, the local Nusselt number (convection-to-conduction heat transfer ratio in the boundary layer), and the local Sherwood number (convection-to-diffusion mass transfer ratio).



(a) (b)

Fig. 15 Effect of *(a)*Eyring-Powell fluid parameter(δ) and *(b)* curvature parameterγ on the flow skin friction coefficient

.

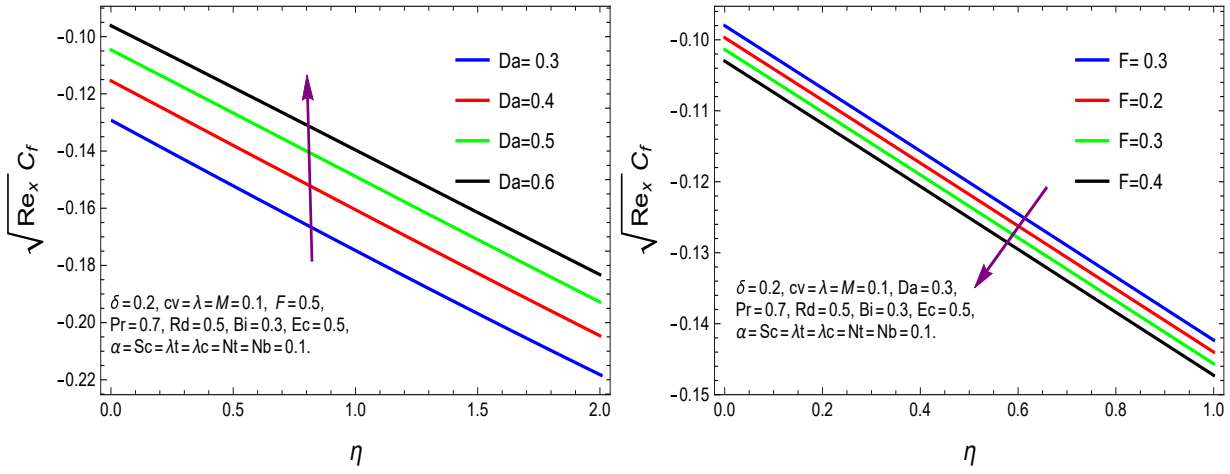


(a) (b)

Fig. 16 Effect of *(a)* Magnetic parameter(M) and *(b)* fluid parameter(λ) on the flow skin friction coefficient .

The graph that shows the variation of skin friction coefficient C_f with respect to δ is illustrated in Fig.**??**, whereas the impact of the curvature parameter γ on the skin friction coefficient is demonstrated in Fig.15b. From Fig.15b, it is evident that the skin friction coefficient reduces with increasing value of γ.

The Fig.16a portrays the impact of the magnetic parameter on the skin friction coefficient C_f. It can be seen that C_f decreases sharply with an increase in the value of the magnetic parameter. In physical terms, the application of the transverse magnetic field results in the generation of a Lorentz force that acts against the flow of an electrically conducting fluid, acting like a body force due to resistivity. As a result of such damping effect of magnetism, the gradient of velocity at the wall is reduced, leading to a reduction of wall shear stress. This results in weakening of the momentum transfer within the boundary layer and thickening of the velocity boundary layer and hence lowering of the surface friction. Fig.16b shows the impact of the fluid parameter (λ) on the skin friction coefficient. It is observed that with an increase in the value of λ, the value of C_f increases. In physical terms, the value of λ reflects the rheological characteristics of a fluid. An increase in the value of λ means that the effective viscosity and resistance of the fluid increase, resulting in increased momentum transfer in the boundary layer.



(a) (b)

Fig. 17 Effect of *(a)* Darcy number (Da) and *(b)* Forchheimer parameter (F) on the skin-friction coefficient.

Fig.17a represents the graph of the effect of the Darcy number (Da) on the variation of the skin friction coefficient. The Darcy number represents the permeability of the porous medium, and its variation has a major impact on the nature of momentum transfer within the boundary layer. The increase in the value of the Darcy number results in an increase in the permeability of the porous medium. Therefore, there is a decrease in the drag resistance applied by the porous medium on the fluid flow. From a physics point of view, it has been found that the increase in the value of the Darcy number causes momentum diffusion near the wall. Fig.17b represents the effect of the Forchheimer parameter (F) on the skin friction coefficient. The Forchheimer parameter takes into consideration the nonlinear inertial resistance in a porous medium in the case of moderate to high flow velocities, in addition to the classical Darcy law. As depicted from the results obtained, the skin friction coefficient diminishes as the Forchheimer parameter (F) is increased. An increase in the Forchheimer parameter implies an increase in the nonlinear resistance against the flow in the porous medium, which causes a decrease in fluid flow close to the surface. Consequently, the skin friction coefficient is reduced as the Forchheimer parameter is increased.

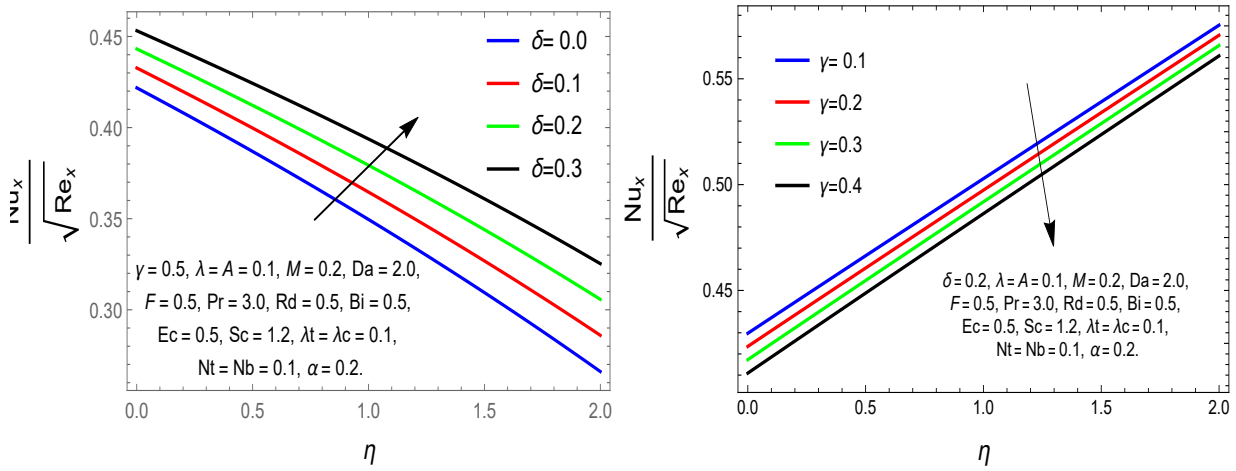


Fig. 18 Effect of *(a)* Eyring-Powell fluid parameter(δ) and *(b)* Cylinder curvature parameter(γ) on the flow Nusselt number(heat rate transfer).

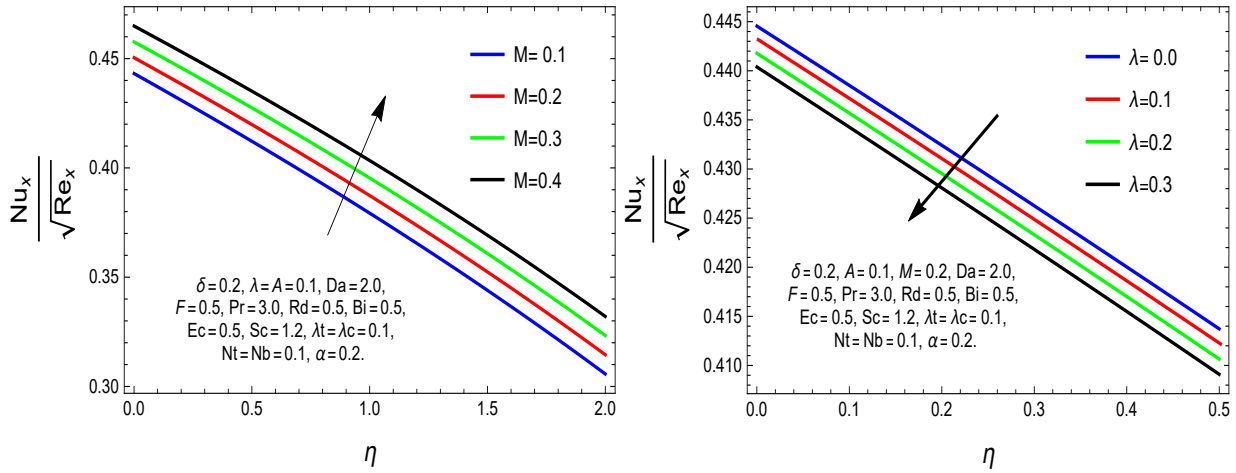


Fig. 19 Effect of *(a)* Magnetic parameter (M) and *(b)* fluid parameter(λ) on the flow Nusselt number(heat transfer rate)

Figs.18a - 18b illustrate the influence of the Eyring-Powell fluid parameter δ and curvature parameter γ on the local Nusselt number. From these figures, one can see that an increment in δ increases the heat transfer rate, whereas an increase in γ results in a decrease in the local Nusselt number. From Fig. 19a, it is evident that an increment in the magnetic parameter M increases the local Nusselt number (or heat transfer rate). But from Fig. 19b, it is noted that an increment in the fluid parameter λ decreases the heat transfer rate of the flow.

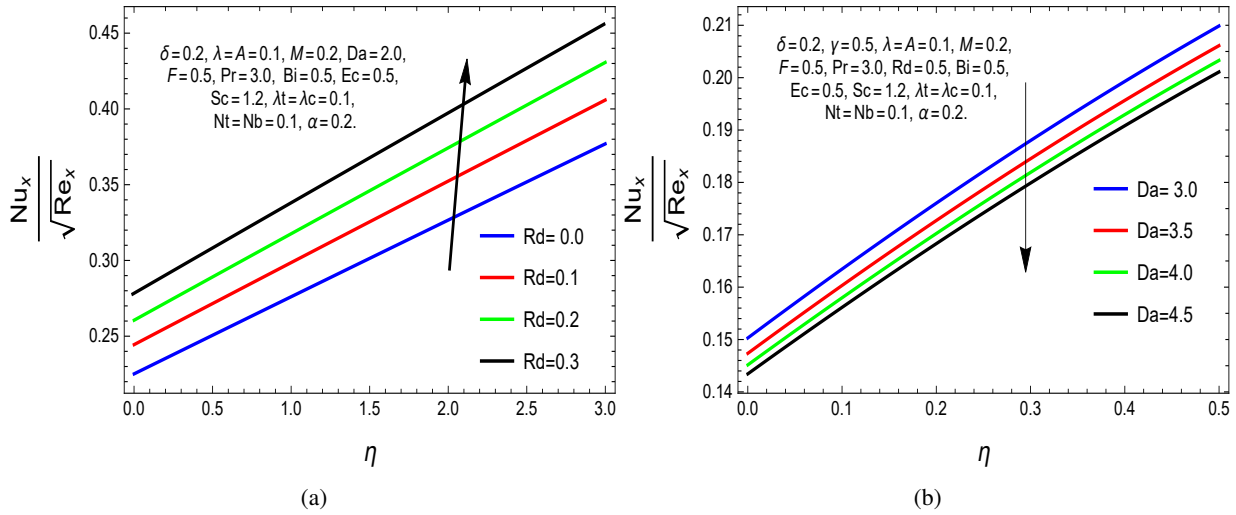


Fig. 20 Effect of *(a)* Radiation parameter(Rd) and *(b)* Darcy number (Da) on the flow Nusselt number(heat transfer rate).

The relationship between the Nusselt number Nu (heat transfer rate) and the thermal radiation parameter Rd can be observed in Fig.20a. It is evident from Fig. 20a that as the value of Rd increases, the heat transfer rate increases too. On the other hand, it can be seen from Fig.20b that the Nusselt number decreases with increasing Darcy number (Da) in the presence of thermal radiation effects.

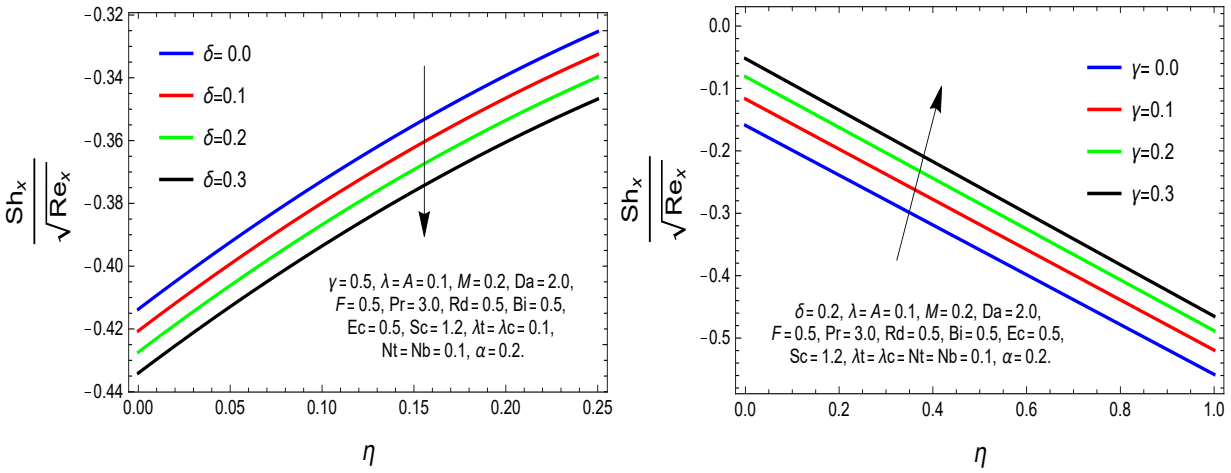


Fig. 21 Effect of *(a)* Eyring-Powell fluid parameter (δ) and *(b)* cylinder curvature parameter(γ) on the flow Sherwood number(mass transfer rate

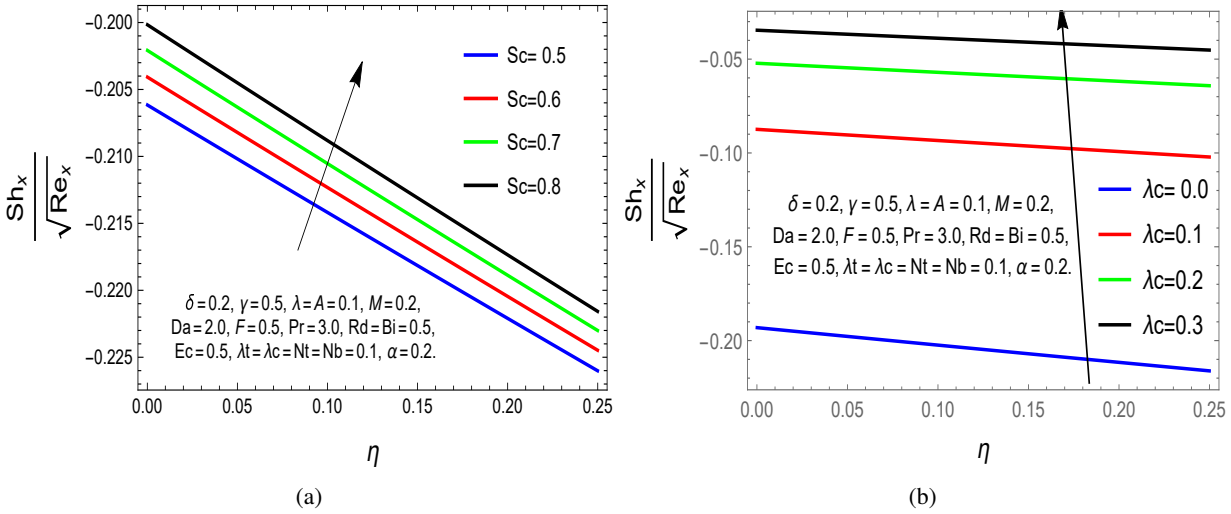


Fig. 22 Effect of *(a)* solutal relaxation time (λ_C) parameter and *(a)* Schmidt number (Sc) On the flow Sherwood number(mass transfer rate)

As evident from Fig.22a, there is a relation between Schmidt number (Sc) and the mass transfer rate, which is the ratio of momentum diffusivity to mass diffusivity. Higher Sc values mean lower mass diffusivity and hence, a thinner concentration boundary layer. Consequently, this results in a steeper concentration gradient and higher rate of mass transfer. The physical explanation for higher Sc values is that high Sc values limit diffusion of the species away from the wall and cause more accumulation of the solute near the wall. In this way, mass transfer rate increases. As shown in Fig.22b, the solutal relaxation time parameter (λ_c) in the non-Fickian mass diffusion models represents the finite time delay for the solute flux response to the concentration gradient. Higher λ_c values indicate more memory effects in the solute transport process. Higher λ_c values lead to a thinner solutal boundary layer.

Table 1 Comparison of the skin-friction coefficient $\sqrt{Re_x}c_f$ of the present results with the previously published results of [10, 25] for $\gamma = 0$ and $M = 0$.

$\sqrt{Re_x}c_f = 2\left[(1+\delta)f''(0) - \frac{1}{3}\delta\lambda(f''(0))^3\right]$				
λ	δ	[25]	[10] (RK45)	**Present (HAM)**
0.0	0.0	-1.00000	–	**-1.00000**
	0.2	-1.09545	–	**-1.09240**
	0.4	-1.18322	–	**-1.18320**
	0.6	-1.26491	–	**-1.26492**
	0.8	-1.34164	–	**-1.34165**
	1.0	-1.41421	–	**-1.41425**
0.1	0.2	-1.09395	-1.09400	**-1.09396**
	0.4	-1.18054	–	**-1.18054**
	0.6	-1.26199	–	**-1.26196**
	0.8	-1.33838	–	**-1.33837**
	1.0	-1.41073	–	**-1.41073**
0.2	0.2	-1.09245	-1.09250	**-1.09246**
	0.4	-1.17843	–	**-1.17846**
	0.6	-1.25902	–	**-1.25903**
	0.8	-1.33506	–	**-1.33505**
	1.0	-1.40718	–	**-1.40717**
0.3	0.2	-1.09092	-1.09090	**-1.09091**
	0.4	-1.17846	–	**-1.17599**
	0.6	-1.26200	–	**-1.25292**
	0.8	-1.33167	–	**-1.33166**
	1.0	-1.40718	–	**-1.40717**
0.4	0.2	-1.08938	-1.08940	**-1.08938**
	0.4	-1.17349	–	**-1.17350**
	0.6	-1.25291	–	**-1.25292**
	0.8	-1.32821	–	**-1.32820**
	1.0	-1.39990	–	**-1.39980**
0.5	0.2	-1.08782	-1.08780	**-1.08783**
	0.4	-1.17096	–	**-1.17099**
	0.6	-1.24976	–	**-1.24981**
	0.8	-1.32467	–	**-1.32466**
	1.0	-1.39609	–	**-1.39607**

The convergence of the series solutions for the governing momentum equations, as shown in Table 1, indicates that acceptable convergence is achieved at the 5^{th} and 10^{th} order approximations. In this table, the skin friction coefficient is compared with results from previously published studies [10, 25] for the case γ=M=0. The comparison shows good agreement between the present results and those reported in the literature. Furthermore, it is observed that the skin friction coefficient increases with increasing values of the magnetic parameter M, whereas larger values of the fluid parameter λ lead to a decrease in the skin friction coefficient.

5 Concluding remarks and perspectives

In the present study, the impact of the Darcy-Forchheimer phenomenon, Cattaneo-Christov heat flux, convection, thermal radiation, and chemical reaction on the Powell-Eyring fluid over a stretching cylinder in the presence of a magnetic field is analyzed through an adaptive technique. The major results of the present study can be summarized as follows:

- Velocity distribution and the momentum boundary layer thickness increase with the increase in the values of the Eyring-Powell fluid parameter(δ), curvature parameter of the cylinder(γ), and velocity ratio parameter(A).
- Temperature distribution and thickness of the thermal boundary layer increase with the increase in radiation parameter (Rd), Darcy Forchheimer parameter(F), Biot number(Bi), and Eckert number(Ec).

- With the increase in the cylinder curvature parameter(γ) and the Eyring-Powell fluid parameter(δ), the velocity, temperature, and concentration of the nanofluid increase.
- Skin friction coefficient (Cf) increases with an increase in the Eyring-Powell fluid parameter and Darcy number(Da)
- Thermal radiation parameter(Rd) increases with an increase in the Nusselt number(Nu), whereas the thermal relaxation time(λ_t) reduces the Nusselt number.
- With an increase in the Schmidt number (Sc) and solutal relaxation time(λ_c), the Sherwood number(Sh) increases.
- The correctness of the current research is justified based on comparison with previous studies using quantitative data.

Nomenclature

A	Velocity ratio parameter
Bi	Biot number
B_0	Magnetic field strength
C_f	Skin-friction coefficient
C_s	Concentration susceptibility
Da	Darcy number
D_B	Brownian diffusion coefficient ($\mathrm{m^2\,s^{-1}}$)
D_T	Thermal diffusion coefficient ($\mathrm{m^2\,s^{-1}}$)
Ec	Eckert number
J	Mass flux ($\mathrm{kg\,m^{-2}\,s^{-1}}$)
K	Porous parameter
F	Forchheimer parameter
Rd	Radiation parameter
K_T	Thermal diffusion ratio
M	Magnetic parameter
Nu_x	Local Nusselt number
Nt	Thermophoresis parameter
Nb	Brownian motion parameter
q_r	Radiative heat flux ($\mathrm{W\,m^{-2}}$)
Pr	Prandtl number
h_f	Convective heat transfer coefficient ($\mathrm{W\,m^{-2}\,K^{-1}}$)
K_r	Chemical reaction rate ($\mathrm{s^{-1}}$)
k^*	Stefan–Boltzmann constant ($\mathrm{W\,m^{-2}\,K^{-4}}$)
R	Cylinder radius (m)
Sc	Schmidt number
Sh_x	Local Sherwood number
T_w	Wall temperature (K)
T_∞	Ambient temperature (K)
$(\rho c_p)_p$	Heat capacity of nanoparticles ($\mathrm{J\,m^{-3}\,K^{-1}}$)
$(\rho c_p)_f$	Heat capacity of the base fluid ($\mathrm{J\,m^{-3}\,K^{-1}}$)
(u,v)	Velocity components ($\mathrm{m\,s^{-1}}$)

Greek symbols

δ	Eyring–Powell fluid parameter
γ	Curvature parameter
F	Forchheimer constant
λ_E	Coefficient of thermal expansion ($\mathrm{K^{-1}}$)
λ_C	Coefficient of concentration expansion ($\mathrm{m^3\,kg^{-1}}$)
σ^*	Rosseland mean absorption coefficient ($\mathrm{m^{-1}}$)
Γ	Heat capacity ratio
α_f	Thermal diffusivity of the fluid ($\mathrm{m^2\,s^{-1}}$)
μ	Dynamic viscosity (Pa s)
α	Chemical reaction parameter ($\mathrm{s^{-1}}$)
λ	Fluid parameter
η	Similarity variable
λ_t	Thermal relaxation time parameter
λ_c	Solutal relaxation time parameter
ψ	Stream function ($\mathrm{m^2\,s^{-1}}$)
σ	Electrical conductivity of the fluid ($\mathrm{S\,m^{-1}}$)
θ	Dimensionless temperature
ϕ	Dimensionless nanoparticle concentration

Author contributions

All authors contributed to the study conception and design. The problem formulation, scheme development, and first draft of the manuscript were written by E.H. The numerical experimentation and supervision were conducted by J.S. All authors read and approved the final manuscript.

Funding

There is no fund support for this research work

Data Availability

The datasets generated during and/or analysed during the current study are available from the corresponding author on reasonable request.

Declarations

Ethics approval and consent to participate

Not applicable

Consent for publication

Not applicable.

Competing interests

The authors declare that they have no competing interests.

References

1. Sakiadis, B.C.: Boundary-layer behavior on continuous solid surfaces: I. boundary-layer equations for two-dimensional and axisymmetric flow. AIChE Journal **7**(1), 26–28 (1961) https://doi.org/10.1002/aic.690070108

2. Crane, L.J.: Flow past a stretching plate. Zeitschrift für angewandte Mathematik und Physik **21**(4), 645–647 (1970) https://doi.org/10.1007/BF01587695

3. Misra, S., Kamatam, G.: Effect of magnetic field, heat generation and absorption on nanofluid flow over a nonlinear stretching sheet. Beilstein Journal of Nanotechnology **11**(1), 976–990 (2020) https://doi.org/10.3762/bjnano.11.82

4. Nithya, N., Vennila, B.: Mhd nanofluid boundary layer flow over a stretching sheet with viscous, ohmic dissipation. Mathematical Modeling and Computing **10**(1), 195–203 (2023) https://doi.org/10.23939/mmc2023.01.195

5. Zafar, S., Zaib, A., Faizan, M., Shah, N.A., Ali, F., Yook, S.-J.: Bioconvection flow of prandtl nanomaterial due to stretched cylinder enclosed through darcy forchheimer flow with triple stratification. Alexandria Engineering Journal **116**, 188–201 (2025) https://doi.org/10.1016/j.aej.2024.12.062

6. Abdelsalam, S.I., Ali, F., Zafar, S., Faizan, M., Shah, N.A., Saeed, A.M.: Homann modeling of thermodynamic optimization on yield-stress nanofluid with radiation and bioconvection effects. Modern Physics Letters B **40**(14), 2650092 (2026) https://doi.org/10.1142/S0217984926500922

7. Danny, M., Kafunda, T., Christian, K., Stanley, J.: Analysis on heat and mass transfer in boundary layer non-newtonian nanofluid flow past a vertically stretching porous plate with chemical reaction, variable magnetic field and variable thermal conductivity. International Journal of Advanced Applied Mathematics and Mechanics **11**(4), 1–14 (2024) https://doi.org//creativecommons.org/licenses/by-nc-nd/3.0/

8. Ferdows, M., Shamshuddin, M., Salawu, S., Sun, S.: Thermal cooling performance of convective non-newtonian nanofluid flowing with variant power-index across moving extending surface. Scientific reports **12**(1), 8714 (2022) https://doi.org/10.1038/s41598-022-12333-y

9. Salah, F.: Chemical reaction and generalized heat flux model for powell–eyring model with radiation effects. International Journal of Mathematics and Mathematical Sciences **2022**(1), 4076426 (2022) https://doi.org/10.1016/j.ijft.2024.101000

10. Rikitu, E.H.: Flow dynamics of eyring–powell nanofluid on porous stretching cylinder under magnetic field and viscous dissipation effects. Advances in Mathematical Physics **2023**(1), 9996048 (2023) https://doi.org/10.1155/2023/9996048

11. Arafat, H., Anjum, A., Zafar, S., Ahmed, M.F., Ali, F., Saeed, A.M., Sidi, H.O., Khidhi, D.M., Shah, N.A.: Entropy generation in radiative bioconvective maxwell nanofluid flow influenced by lorentz force and darcy–forchheimer porous rotating disk. Journal of Radiation Research and Applied Sciences **18**(4), 101993 (2025) https://doi.org/10.1016/j.jrras.2025.101993

12. Loganathan, K., Thamaraikannan, N., Eswaramoorthi, S., Jain, R.: Entropy framework of the bioconvective williamson nanofluid flow over a riga plate with radiation, triple stratification and swimming microorganisms. International Journal of Thermofluids **25**, 101000 (2025) https://doi.org/10.1016/j.ijft.2024.101000

13. Abdelsalam, S.I., Shah, N.A., Zafar, S.S., Ali, F., Khalifa, S.B., Chebaane, S., Saidani, T., Faizan Ahmed, M.: Microbial bioconvection transport across darcy–forchheimer cylindrical geometries in nanofluid flow. Modern Physics Letters B **39**(35), 2550227 (2025) https://doi.org/10.1142/S0217984925502276

14. Akinbo, B.: Irreversibility analysis of hydromagnetic flow in a nonlinearly radiating walters' b fluid through a porous medium with thermal buoyancy influence and viscous dissipation. Transport in Porous Media **152**(11), 96 (2025) https://doi.org/0.1007/s11242-025-02234-9

15. Akinbo, B., Olajuwon, B.: Impact of radiation and chemical reaction on stagnation-point flow of hydromagnetic walters' b fluid with newtonian heating. International Communications in Heat and Mass Transfer **121**, 105115 (2021) https://doi.org/10.1016/j.icheatmasstransfer.2021.105115

16. Reddy, M.V., Ajithkumar, M., Ali, F., Reddy, K.V., Khan, U.: Entropy optimization in magneto nonlinear mixed convective flow of ree-eyring nanofluid with activation energy and gyrotactic microorganisms. Journal of Nonlinear Mathematical Physics **32**(1), 47 (2025) https://doi.org/10.1007/s44198-025-00300-w

17. Akinbo, B.J., Olajuwon, B.I.: Interaction of radiation and chemical reaction on walters' b fluid over a medium porosity of a vertical stretching surface. Heat Transfer **52**(2), 1689–1709 (2023) https://doi.org/10.1002/htj.22759

18. Akinbo, B., Olajuwon, B.: Significance of cattaneo-christov heat flux model and heat generation/absorption with chemical reaction in walters' b fluid via a porous medium in the presence of newtonian heating. International Journal of Modelling and Simulation **45**(1), 137–146 (2025) https://doi.org/10.1080/02286203.2023.2188513

19. Christov, C.: On frame indifferent formulation of the maxwell–cattaneo model of finite-speed heat conduction. Mechanics research communications **36**(4), 481–486 (2009) https://doi.org/10.1016/j.mechrescom.2008.11.003

20. Alamri, S.Z., Khan, A.A., Azeez, M., Ellahi, R.: Effects of mass transfer on mhd second grade fluid towards stretching cylinder: a novel perspective of cattaneo–christov heat flux model. Physics Letters A **383**(2-3), 276–281 (2019) https://doi.org/10.1016/j.physleta.2018.10.035

21. Rooman, M., Jan, M.A., Shah, Z., Vrinceanu, N., Ferrándiz Bou, S., Iqbal, S., Deebani, W.: Entropy optimization on axisymmetric darcy–forchheimer powell–eyring nanofluid over a horizontally stretching cylinder with viscous dissipation effect. Coatings **12**(6), 749 (2022) https://doi.org/10.3390/coatings12060749

22. Liao, S.: Homotopy Analysis Method in Nonlinear Differential Equations vol. 153. Springer, ??? (2012). https://doi.org/10.1007/978-3-642-25132-0

23. Kumbhakar, M., Singh, V.P.: Homotopy-based Methods in Water Engineering. CRC Press, ??? (2023). https:

//doi.org/10.1201/9781003368984

24. Shah, N.A., Ali, F., Faizan, M., Zafar, S.: Theoretical exploration of bioconvection magneto flow of micropolar nanomaterial off-centered stagnation point framed by rotating disk. Advanced Theory and Simulations **8**(6), 2401345 (2025) https://doi.org/10.1002/adts.202401345

25. Sekhar, P.R., Sreedhar, S., Ibrahim, S.M., Kumar, P.V.: Radiative heat source fluid flow of mhd casson nanofluid over a non-linear inclined surface with soret and dufour effects. CFD Lett **15**(7), 42–60 (2023) https://doi.org/10.37934/cfdl.15.7.4260